in other subdomains may affect the structure of the MSD. This may have implications for the mechanism of disassembly and for that of uncoating events, and may also suggest that the MSD of gp41 may become another target for therapeutic intervention against HIV-1 infection.

ACKNOWLEDGMENTS

This study was supported by the Health and Labour Sciences Research Grants from Japanese Ministry of Health, Labour and Welfare.

The following reagents were obtained through the AIDS Research and Reference Reagent Program, Division of AIDS, National Institute of Allergy and Infectious Diseases, National Institutes of Health: The hybridoma 902 from Dr. Bruce Chesebro, The hybridoma Chessie 8 from Dr. George Lewis.

We are grateful to M. Segawa, H. Matsushita and H. Yamamoto for purification of the monoclonal antibodies. We thank A. M. Menting for assistance in manuscript preparation.

REFERENCES

1. Chan, D. C., Fass, D., Berger, J. M. and Kim, P. S. (1997): Core structure of gp41 from the HIV envelope glycoprotein. Cell, 89, 263-273.
2. Gallaher, W. R. (1987): Detection of a fusion peptide sequence in the transmembrane protein of human immunodeficiency virus. Cell, 50, 327-328.
3. Eckert, D. M. and Kim, P. S. (2001): Mechanisms of viral membrane fusion and its inhibition. Annu. Rev. Biochem., 70, 777-810.
4. Lu, M., Blacklow, S. C. and Kim, P. S. (1995): A trimeric structural domain of the HIV-1 transmembrane glycoprotein. Nat. Struct. Biol., 2, 1075-1082.
5. Wilk, T., Pfeiffer, T., Bukovsky, A., Moldenhauer, G. and Bosch, V. (1996): Glycoprotein incorporation and HIV-1 infectivity despite exchange of the gp160 membrane-spanning domain. Virology, 218, 269-274.
6. Deml, L., Kratochwil, G., Osterrieder, N., Knuchel, R., Wolf, H. and Wagner, R. (1997): Increased incorporation of chimeric human immunodeficiency virus type 1 gp120 proteins into Pr55gag virus-like particles by an Epstein-Barr virus gp220/350-derived transmembrane domain. Virology, 235, 10-25.
7. Salzwedel, K., Johnston, P. B., Roberts, S. J., Dubay, J. W. and Hunter, E. (1993): Expression and characterization of glycophospholipid-anchored human immunodeficiency virus type 1 envelope glycoproteins. J. Virol., 67, 5279-5288.
8. Munoz-Barroso, I., Salzwedel, K., Hunter, E. and Blumenthal, R. (1999): Role of the membrane-proximal domain in the initial stages of human immunodeficiency virus type 1 envelope glycoprotein-mediated membrane fusion. J. Virol., 73, 6089-6092.
9. Melikyan, G. B., Lin, S., Roth, M. G. and Cohen, F. S. (1999): Amino acid sequence requirements of the transmembrane and cytoplasmic domains of influenza virus hemagglutinin for viable membrane fusion. Mol. Biol. Cell, 10, 1821-1836.
10. Melikyan, G. B., Markosyan, R. M., Roth, M. G. and Cohen, F. S. (2000): A point mutation in the transmembrane domain of the hemagglutinin of influenza virus stabilizes a hemifusion intermediate that can transit to fusion. Mol. Biol. Cell, 11, 3765-3775.
11. Lin, X., Derdeyn, C. A., Blumenthal, R., West, J. and Hunter, E. (2003): Progressive truncations C terminal to the membrane-spanning domain of simian immunodeficiency virus Env reduce fusogenicity and increase concentration dependence of Env for fusion. J. Virol., 77, 7067-7077.
12. Russ, W. P. and Engelman, D. M. (1999): TOXCAT: a measure of transmembrane helix association in a biological membrane. Proc. Natl. Acad. Sci. USA, 96, 863-868.
13. Fleming, K. G. and Engelman, D. M. (2001): Specificity in transmembrane helix-helix interactions can define a hierarchy of stability for sequence variants. Proc. Natl. Acad. Sci. USA, 98, 14340-14344.
14. Op De Beeck, A., Montserret, R., Duvet, S., Cocquerel, L., Cacan, R., Barberot, B., Le Maire, M., Penin, F. and Dubuisson, J. (2000): The transmembrane domains of hepatitis C virus envelope glycoproteins E1 and E2 play a major role in heterodimerization. J. Biol. Chem., 275, 31428-31437.
15. Kuiken, C., Foley, B., Hahn, B., Marx, P., McCutchan, F., Mellors, J., Wolinsky, S. and Korber, B. (ed.) (2001): HIV Sequence Compendium 2001. Theoretical Biology and Biophysics Group, Los Alamos National Laboratory, N. Mex.
16. Cleverley, D. Z. and Lenard, J. (1998): The transmembrane domain in viral fusion: essential role for a conserved glycine residue in vesicular stomatitis virus G protein. Proc. Natl. Acad. Sci. USA, 95, 3425-3430.
17. Miyauchi, K., Komano, J., Yokomaku, Y., Sugiura, W., Yamamoto, N. and Matsuda, Z. (2005): Role of the specific amino acid sequence of the membrane-spanning domain of human immunodeficiency virus type 1 in membrane fusion. J. Virol., 79, 4720-4729.
18. Chesebro, B. and Wehrly, K. (1988): Development of a sensitive quantitative focal assay for human immunodeficiency virus infectivity. J. Virol., 62, 3779-3788.
19. Pincus, S. H., Wehrly, K. and Chesebro, B. (1989): Treatment of HIV tissue culture infection with monoclonal antibody-ricin A chain conjugates. J. Immunol., 142, 3070-3075.
20. Abacioglu, Y. H., Fouts, T. R., Laman, J. D., Claassen, E., Pincus, S. H., Moore, J. P., Roby, C. A., Kamin-Lewis, R. and Lewis, G. K. (1994): Epitope mapping and topology of baculovirus-expressed HIV-1 gp160 determined with a panel of murine monoclonal antibodies. AIDS Res. Hum. Retroviruses, 10, 371-381.
21. Matsuda, Z., Yu, X., Yu, Q. C., Lee, T. H. and Essex, M. (1993): A virion-specific inhibitory molecule with therapeutic potential for human immunodeficiency virus type 1. Proc. Natl. Acad. Sci. USA, 90, 3544-3548.
22. Armstrong, R. T., Kushnir, A. S. and White, J. M. (2000): The transmembrane domain of influenza hemagglutinin exhibits a stringent length requirement to support the hemifusion to fusion transition. J. Cell Biol., 151, 425-437.
23. Kleiger, G., Grothe, R., Mallick, P. and Eisenberg, D. (2002): GXXXG and AXXXA: common alpha-helical interaction motifs in proteins, particularly in extremophiles. Biochemistry, 41, 5990-5997.
24. Hessa, T., Kim, H., Bihlmaier, K., Lundin, C., Boekel, J., Andersson, H., Nilsson, I., White, S. H. and von Heijne, G. (2005): Recognition of transmembrane helices by the

endoplasmic reticulum translocon. Nature, 433, 377-381.
25. Hawkins, G. D., Cramer, C. J. and Truhlar, D. G. (1995): Pairwise solute descreening of solute charges from a dielectric medium. Chem. Phys. Lett., 246, 122-129.
26. Tsui, V. and Case, D. A. (2000): Molecular dynamics simulations of nucleic acids with a generalized born solvation model. J. Am. Chem. Soc., 122, 2489-2498.

J|A|C|S
ARTICLES
Published on Web 05/24/2006

Computational Simulations of HIV-1 Proteases—Multi-drug Resistance Due to Nonactive Site Mutation L90M

Hirotaka Ode,* Saburo Neya, Masayuki Hata, Wataru Sugiura,† and Tyuji Hoshino‡

Contribution from the Graduate School of Pharmaceutical Sciences, Chiba University, Chiba 263-8522, Japan

Received January 29, 2006; E-mail: odehir@graduate.chiba-u.jp

Abstract: Human immunodeficiency virus type 1 protease (HIV-1 PR) is one of the proteins that currently available anti-HIV-1 drugs target. Inhibitors of HIV-1 PR have become available, and they have lowered the rate of mortality from acquired immune deficiency syndrome (AIDS) in advanced countries. However, the rate of emergence of drug-resistant HIV-1 variants is quite high because of their short retroviral life cycle and their high mutation rate. Serious drug-resistant mutations against HIV-1 PR inhibitors (PIs) frequently appear at the active site of PR. Exceptionally, some other mutations such as L90M cause drug resistance, although these appear at nonactive sites. The mechanism of resistance due to nonactive site mutations is difficult to explain. In this study, we carried out computational simulations of L90M PR in complex with each of three kinds of inhibitors and one typical substrate, and we clarified the mechanism of resistance. The L90M mutation causes changes in interaction between the side chain atoms of the 90th residue and the main chain atoms of the 25th residue, and a slight dislocation of the 25th residue causes rotation of the side chain at the 84th residue. The rotation of the 84th residue leads to displacement of the inhibitor from the appropriate binding location, resulting in a collision with the flap or loop region. The difference in levels of resistance to the three inhibitors has been explained from energetic and structural viewpoints, which provides the suggestion for promising drugs keeping its efficacy even for the L90M mutant.

Introduction

Human immunodeficiency virus type 1 (HIV-1) proliferates under the assistance of its own aspartic protease, so-called HIV-1 protease (PR), in its life cycle.[1] HIV-1 PR is an enzyme composed of two identical polypeptides, each of which consists of 99 amino acid residues (Figure 1A), and has a function to process the viral Gag and Gag-Pol polyprotein precursors. Because this processing is essential for the viral maturation, the inhibition of PR function leads to an incomplete viral replication and prevents the infection of other cells.[2] Therefore, HIV-1 PR is an attractive target for anti-HIV-1 drugs. Seven PR inhibitors (PIs) have been approved by the FDA[3−9] and have successfully lowered the death rate due to acquired immune deficiency syndrome (AIDS) in advanced countries during the past decade. However, the emergence of PI-resistant mutants has become a serious problem in AIDS therapies.[10−13] The accumulation of multidrug-resistant mutations within HIV-1 PR makes it difficult to control viral replication in patients. Hence, PIs that maintain drug efficacy even for drug-resistant mutants are needed.

Most mutations causing a high level of drug resistance occur at the active site of HIV-1 PR. For example, D30N and G48V lead to specific resistance against nelfinavir (NFV) and saquinavir (SQV), respectively, and I84V shows multidrug resistance against several approved PIs.[7,10−18] Recent structural analyses by not only X-ray crystallography[19−28] but also computational

† AIDS Research Center, National Institute of Infectious Diseases, Musashimurayama, Tokyo 208-1011, Japan.
‡ Also PRESTO, JST, 4-1-8 Honcho Kawaguchi, Saitama, Japan.

(1) Kräusslich, H. G.; Wimmer, E. *Auu. Rev. Biochem.* **1988**, *57*, 701.
(2) Kohl, N. E.; Emini, E. A.; Schleif, W. A.; Davis, L. J.; Heimbach, J. C.; Dixon, R. A.; Scolinick, E. M.; Sigal, I. S. *Proc. Natl. Acad. Sci. U.S.A.* **1988**, *85*, 4686.
(3) Craig, J. C.; Duncan, I. B.; Hockley, D.; Grief, C.; Roberts, N. A.; Mills, J. S. *Antiviral Res.* **1991**, *16*, 295.
(4) Vacca, J. P.; et al. *Proc. Natl. Acad. Sci. U.S.A.* **1994**, *91*, 4096.
(5) Kempf, D. J.; et al. *Proc. Natl. Acad. Sci. U.S.A.* **1995**, *92*, 2484.
(6) Livington, D. J.; Pazhanisamy, S.; Porter, D. J.; Partaledis, J. A.; Tung, R. D.; Painter, G. R. *J. Infect. Dis.* **1995**, *172*, 1238.
(7) Patick, A. K.; et al. *Antimicrob. Agents Chemother.* **1996**, *40*, 292 (Erratum, *40*, 1575).
(8) Carrillo, A.; Stewart, K. D.; Sham, H. L.; Norbeck, D. W.; Kohlbrenner, W. E.; Leonard, J. M.; Kempf, D. J.; Molla, A. J. *J. Virol.* **1998**, *72*, 7532.
(9) Robinson, B. S.; et al. *Antimicrob. Agents Chemother.* **2000**, *44*, 2093.
(10) Condra, J. H.; et al. *Nature (London)* **1995**, *374*, 579.
(11) Kantor, R.; Fessel, W. J.; Zolopa, A. R.; Israelski, D.; Shulman, N.; Montoya, J. G.; Harbour, M.; Schapiro, J. M.; Shafer, R. W. *Antimicrob. Agents Chemother.* **2002**, *46*, 1086.
(12) Wu, T. D.; Schiffer, C. A.; Gonzales, M. J.; Taylor, J.; Kantor, R.; Chou, S.; Israelski, D.; Zolopa, A. R.; Fessel, W. J.; Shafer, R. W. *J. Virol.* **2003**, *77*, 4836.
(13) Johnson, V. A.; Brun-Vézinet, F.; Clotet, B.; Conway, B.; Kuritzkes, D. R.; Pillay, D.; Schapiro, J.; Telenti, A.; Richman, D. *Top. HIV Med.* **2005**, *13*, 125.
(14) Patick, A. K.; Duran, M.; Cao, Y.; Shugarts, D.; Keller, M. R.; Mazabel, E.; Knowles, M.; Chapman, S.; Kuritzkes, D. R.; Markowitz, M. *Antimicrob. Agents Chemother.* **1998**, *42*, 2637.
(15) Jacobsen, H.; Yasargil, K.; Winslow, D. L.; Craig, J. C.; Krohn, A.; Duncan, I. B.; Mous, J. *Virology* **1995**, *206*, 527.
(16) Jacobsen, H.; Hänggi, M.; Ott, M.; Duncan, I. B.; Andreoni, M.; Vella, S.; Mous, J. *Antiviral Res.* **1996**, *29*, 95.
(17) Jaconsen, H,; Hänggi, M.; Ott, M.; Duncan, I. B.; Owen, S.; Andreoni, M.; Vella, S.; Mous, J. *J. Infect. Dis.* **1996**, *173*, 1379.
(18) Ermolieff, J.; Lin, X.; Tang. J. *Biochemistry* **1997**, *36*, 12364.
(19) Mahalingam, B.; Louis, J. M.; Reed, C. C.; Adomat, J. M.; Krouse, J.; Wang, Y.-F.; Harrison, R. W.; Weber, I. T. *Eur. J. Biochem.* **1999**, *263*, 238.
(20) Hong, L.; Zhang, X. C.; Hartsuck, J. A.; Tang, J. *Protein Sci.* **2000**, *9*, 1898.

10.1021/ja060682b CCC: $33.50

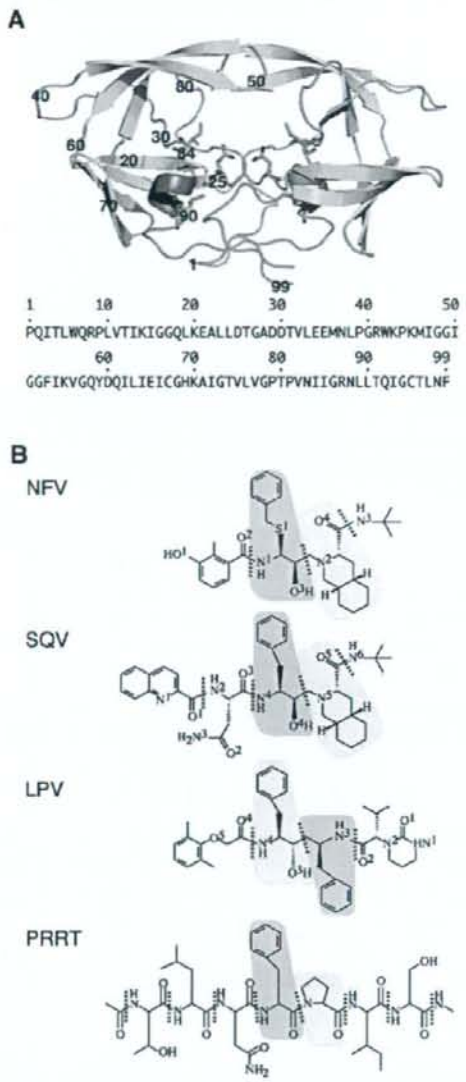

Figure 1. A: Structure of HIV-1 PR. Locations of the two catalytic aspartates, the 84th and the 90th residues, are shown in stick representation. The WT sequence of HIV-1 PR is shown below. B: Chemical structures of NFV, SQV, LPV, and PRRT. Each red dotted line shows a junction between subsites. The P1 subsite is highlighted with an orange background, and the P1′ subsite is highlighted with a yellow background.

studies[29–34] have revealed that these active site mutations changed direct interactions between PR and PI and caused unfavorable contact between them. Nonactive site mutations such as L10F and L90M have also been reported to cause a high level of resistance, although these residues cannot directly interact with PIs.[7,10–18] It is difficult to understand how nonactive site mutations lead to resistance against PIs. L90M is a primary mutation responsible for resistance against NFV and SQV.[7,14–17] L90M also appears to be associated with resistance to other PIs.[11–13] The structures of L90M PR mutants in complex with PIs have been determined through X-ray crystallographic approaches by some groups[20,26] and through our previous computational simulations.[33] These structures showed that the side chains of the mutated M90/M90′ altered their interactions with the catalytic aspartates D25/D25′. Additionally, L90M mutation affected local conformations at the 80's loop of PR, which is quite far from the location of the 90th residues. The mechanism of resistance due to L90M, however, is still not clear, and a strategy for the design of potent drugs against L90M-acquired virus has not yet been established.

In this study, we carried out computational simulations of L90M PR in complex with several kinds of ligands to clarify the mechanism of resistance due to L90M. NFV, SQV, and lopinavir (LPV) were selected as representative PI inhibitors currently used in the clinical field (Figure 1B). NFV and SQV lose their ability to inhibit PRs that have acquired L90M mutation. In contrast, single mutations have little effect on the inhibition ability of LPV.[35] In addition, the oligopeptide at the PR/RT cleavage site (PRRT) was selected as a typical substrate for the enzyme to investigate the effect of L90M on substrate binding (Figure 1B). The PR/RT cleavage site contains Phe-Pro at the P1−P1′ residues (notation by Schecter and Berger[36]). It is unusual for mammalian endopeptidases to cleave the peptide bond located at the N-terminal side of Pro, and this cleavage site is specific to HIV-1 PR.[37,38] This cleavage mechanism is unique as reported previously.[39–41] Therefore, the structure of PRRT was used as the base of drug design for NFV, SQV, and some PIs.[3,7,42] In this study, the binding energies of NFV, SQV, LPV, and PR/RT were first calculated to compare the levels of resistance of the wild type (WT) and L90M mutant. The binding structures were then compared in two groups of inhibitors: one groups consisting of HIV inhibitors that lose drug efficacy due

(21) Mahalingam, B.; Louis, J. M.; Hung, J.; Harrison, R. W.; Weber, I. T. *Proteins* **2001**, *43*, 455.
(22) Mahalingam, B.; Boross, P.; Wang, Y.-F.; Louis, J. M.; Fischer, C. C.; Tozser, J.; Harrison, R. W.; Weber, I. T. *Proteins* **2002**, *48*, 107.
(23) Weber, J.; et al. *J. Mol. Biol.* **2002**, *324*, 739.
(24) King, N. M.; Melnick, L.; Prabu-Jeyabalan, M.; Nalivaika, E. A.; Yang, S. S.; Gao, Y.; Nie, X.; Zepp, C.; Heefner, D. L.; Schiffer, C. A. *Protein Sci.* **2002**, *11*, 418.
(25) Prabu-Jeyabalan, M.; Nalivaika, E. A.; King, N. M.; Schiffer, C. A. *J. Virol.* **2003**, *77*, 1306.
(26) Mahalingam, B.; Wang, Y.-F.; Boross, P. I.; Tozser, J.; Louis, J. M.; Harrison, R. W.; Weber, I. T. *Eur. J. Biochem.* **2004**, *271*, 1516.
(27) King, N. M.; Prabu-Jeyabalan, M.; Nalivaika, E. A.; Wigerinck, P.; Béthune, M. P.; Schiffer, C. A. *J. Virol.* **2004**, *78*, 12012.
(28) Prabu-Jeyabalan, M.; Nalivaika, E. A.; King, N. M.; Schiffer, C. A. *J. Virol.* **2004**, *78*, 12446.
(29) Rick, S. W.; Topol, I. A.; Erickson, J. W.; Burt, S. K. *Protein Sci.* **1998**, *8*, 1750.
(30) Piana, S.; Carloni, P.; Rothlisberger, U. *Protein Sci.* **2002**, *11*, 2393.
(31) Clemente, J. C.; Hermrajani, R.; Blum, L. E.; Goodenow, M. M.; Dunn, B. M. *Biochemistry* **2003**, *42*, 15029.
(32) Perryman, A. L.; Lin, J.-H.; McCammon, J. A. *Protein Sci.* **2003**, *13*, 1108.
(33) Ode, H.; Ota, M.; Neya, S.; Hata, M.; Sugiura, W.; Hoshino, T. *J. Phys. Chem. B* **2005**, *109*, 565.
(34) Wittayanarakul, K.; Aruksakunwong, O.; Saen-oon, S.; Chantratita, W.; Parasuk, V.; Sompornpisut, P.; Hannongbua, S. *Biophys. J.* **2005**, *88*, 867.
(35) Kempf, D. J.; Isaacson, J. D.; King, M. S.; Brun, S. C.; Xu, Y.; Real, K.; Bernstein, B. M.; Japour, A. J.; Sun, E.; Rode, R. A. *J. Virol.* **2001**, *75*, 7462.
(36) Schechter, I.; Berger, A. *Biochem. Biophys. Res. Commun.* **1967**, *27*, 157.
(37) Pearl, L. H.; Taylor, W. R. *Nature (London)* **1987**, *328*, 482.
(38) Darke, P. L.; Nutt, R. F.; Brady, S. F.; Garsky, V. M.; Ciccarone, T. M.; Leu, C.-H.; Lumma, P. K.; Freidinger, R. M.; Veber, D. F.; Sigal, I. S. *Biochem. Biophys. Res. Commun.* **1988**, *156*, 297.
(39) Okimoto, N.; Tsukui, T.; Hata, M.; Hoshino, T.; Tsuda, M. *J. Am. Chem. Soc.* **1999**, *121*, 7349.
(40) Okimoto, N.; Tsukui, T.; Kitayama, K.; Hata, M.; Hoshino, T.; Tsuda, M. *J. Am. Chem. Soc.* **2000**, *122*, 5613.
(41) Okimoto, N.; Kitayama, K.; Hata, M.; Hoshino, T.; Tsuda, M. *J. Mol. Struct. (THEOCHEM)* **2001**, *543*, 53.
(42) Roberts, N. A.; et al. *Science* **1990**, *248*, 358.

to L90M mutations, such as NFV and SQV, and the other group consisting of drugs that maintain efficacy, such as LPV. Prominent differences between the two groups were seen at the contact of M90 to D25, shifts of D25, rotation of the side chains of I84, displacement of the flap region of I50, and deformation of the loop region of P81. D25, I84, I50, and P81 are all located at the active site of the PR. Detail discussion are developed in contrast with the resistivity of PR. Our findings provide information for designing better inhibitors that maintain drug efficacy despite L90M or other nonactive site mutations.

Materials and Methods

Molecular Dynamics Simulation. Before carrying out molecular dynamics (MD) simulations, quantum chemical calculations were executed for PIs to deduce the atom charges utilized in MD simulations. Geometry optimization was performed on each PI, and the electrostatic potential was calculated at the B3LYP/6-31G(d,p) level using the Gaussian03 program.[43] The partial atom charges were determined using the RESP method[44] so that the atom charges could reproduce the values of the calculated electrostatic potential at the surrounding points of the PI. Charges were set equal between two atoms if they were the same element and had the same bond coordination. Minimizations and MD simulations were carried out using the Sander module of the AMBER7 package.[45] The AMBER ff02 force field[46] was used as the parameters for van der Waals and bonded energy terms basically, and the general AMBER force field[47] was used as the parameters for NFV, SQV, and LPV.

Each initial structure for the clade B HXB2 PRs in complex with NFV, SQV, and LPV was modeled from the atom coordinates of the X-ray crystal structure (PDB code: 1OHR,[48] 1HXB,[42,49] and 1MUI,[50] respectively) using the LEaP module (Figure 1A). The initial structure for the PR in complex with PRRT before the catalytic reaction was modeled in the same manner as that previously reported.[39] The oligopeptide of ACE-THR-LEU-ASN-PHE-PRO-ILE-SER-NME was utilized as PRRT, and one water molecule was inserted between PRRT and D25/D25′. Each model was placed in a rectangular box filled with about 8000 TIP3P water molecules,[51] with all of the crystal water molecules remaining. One water molecule was added between LPV and I50/I50′ in the LPV complex model, because no crystal water molecule was present in the crystallographic data. It is known that the hydrogen bonds between PI and I50/I50′ via the water molecule are critically important for PI binding with HIV-1 PR.[33,39-41] The cutoff distance for the long-range electrostatic and the van der Waals energy terms was set at 12.0 Å. All covalent bonds to hydrogen atoms were constrained using the SHAKE algorithm.[52] Periodic boundary conditions were applied to avoid edge effects in all calculations. Energy minimization was achieved in three steps. At first, movement was allowed only for the water molecules and ions. Next, the ligand and the mutated residues were allowed to move in addition to the water molecules and ions. Finally, all atoms were permitted to move freely. In each step, energy minimization was executed by the steepest descent method for the first 1000 steps and the conjugated gradient method for the subsequent 3000 steps. After 52.0 ps heating calculation until 300 K using the NVT ensemble, 1.5 ns equilibrating calculation was executed at 1 atm and at 300 K using the NPT ensemble, with an integration time step of 1.0 fs. In the present calculations, the MD simulations showed no large fluctuations after about 500 ps equilibrating calculation (Supporting Information Fig. S1). Hence, atom coordinates were collected at the interval of 0.5 ps for the last 500 ps to analyze the structure in detail.

Protonation States. The protonation states of catalytic aspartates D25 and D25′ vary depending on the binding inhibitors or substrates. Hence, the appropriate protonation states of catalytic aspartates should be determined for the respective ligands. For NFV, the protonated state was already determined in our previous study.[33] That is, D25 was protonated and D25′ was unprotonated in each of WT PR and L90M PR in complex with NFV. To determine the protonation states when SQV or LPV binds to the WT PR, the total energies of the two kinds of complexes were compared after energy minimization. One complex represented a combination of protonated D25/unprotonated D25′ states, and the other represented the opposite combination. This comparison clearly suggested the preference of the protonated D25 and unprotonated D25′ states (Supporting Information Table S1 A). In contrast to the case of WT PR, we used another method to determine the protonation states of L90M PR with SQV or LPV because they might have greatly different conformation from the respective crystal structures. Hence, we executed 1.5 ns MD simulations of the two protonation states in these models and compared the total energies of the two protonation states for the last 500 ps of the simulations. The energy comparison indicated that L90M PR in complex with each of SQV and LPV preferred the protonated D25 and unprotonated D25′ states (Supporting Information Table S1 B). For both WT and L90M PR with PRRT, the D25 unprotonated and D25′ protonated states were selected so that the hydrolysis reaction could proceed as described in a previous paper.[39]

Binding Energy Calculation (MM/PBSA). The binding free energy[53] was calculated by the following equation:

$$\Delta G_b = \Delta G_{MM} + \Delta G_{sol} - T\Delta S$$

where ΔG_b is the binding free energy in solution, ΔG_{MM} is the molecular mechanics (MM) interaction energy, ΔG_{sol} is the solvation energy, and $-T\Delta S$ is the contribution of conformational entropy to the binding. Since the contribution of conformational entropy to the change of ΔG_b is negligible among the mutants as pointed out by Massova,[54] the last entropy term in the energy estimation was neglected. ΔG_{MM} was calculated by the following equation:

$$\Delta G_{MM} = \Delta G_{int}^{ele} + \Delta G_{int}^{vdw}$$

where ΔG_{int}^{ele} and ΔG_{int}^{vdw} are electrostatic and van der Waals interaction energies between a ligand and a protein. These energies were computed using the same parameter set as that used in the MD simulation, and no cutoff was applied for the calculation. Solvation energy ΔG_{sol} can be divided into two parts:

$$\Delta G_{sol} = \Delta G_{sol}^{ele} + \Delta G_{sol}^{nonpol}$$

The electrostatic contribution to the solvation free energy (ΔG_{sol}^{ele}) was calculated by the Poisson−Boltzmann (PB) method using the DelPhi program.[55] The hydrophobic contribution to the solvation free energy (ΔG_{sol}^{nonpol}) was determined with a function of the solvent-accessible surface-area.[56]

Hydrogen Bond Criterion. The formation of a hydrogen bond was defined in terms of distance and orientation. The combination of donor

(43) Frisch, M. J.; et al. *Gaussian 03*; Gaussian, Inc., Wallingford CT, 2004.
(44) Cieplak, P.; Cornell, W. D.; Bayly, C.; Kollman, P. A. *J. Comput. Chem.* **1995**, *16*, 1357.
(45) Case, D. A.; et al. *AMBER 7*; University of California: San Francisco, 2002.
(46) Wang, J.; Cieplak, P.; Kollman, P. A. *J. Comput. Chem.* **2000**, *21*, 1049.
(47) Wang, J.; Wolf, R. M.; Caldwell, J. W.; Kollman, P. A.; Case, D. A. *J. Comput. Chem.* **2004**, *25*, 1157.
(48) Kaldor, S. W.; et al. *J. Med. Chem.* **1997**, *40*, 3979.
(49) Krohn, A.; Redshaw, S.; Ritchie, J. C.; Graves, B. J.; Hatada, M. H. *J. Med. Chem.* **1991**, *34*, 3340.
(50) Stoll, V.; et al. *Bioorg. Med. Chem.* **2002**, *10*, 28032.
(51) Jorgensen, W. L.; Chandrasekhar, J.; Madura, J. D.; Impey, R. W.; Klein, M. L. *J. Chem. Phys.* **1983**, *79*, 926.
(52) Ryckaert, J.-P.; Ciccotti, G.; Berendsen, H. J. C. *J. Comput. Phys.* **1977**, *23*, 327.
(53) Kollman, P. *Chem. Rev.* **1993**, *93*, 2395.
(54) Massova, I.; Kollman, P. A. *Perspect. Drug. Discovery Des.* **2000**, *18*, 113.
(55) Honig, B.; Nicholls, A. *Science* **1995**, *268*, 1144.
(56) Sitkoff, D.; Sharp, K. A.; Honig, B. *J. Phys. Chem.* **1994**, *98*, 1978.

Table 1. Binding Energies of Each Model[a]

		ΔG_{vd}^{gas}	ΔG_{vd}^{solv}	ΔG_{ax}	ΔG_b[a]	ΔG_b[c]	resistant level[d]
NFV	WT	−24.4 ± 3.6	−66.6 ± 3.6	37.5 ± 3.3	−53.5 ± 4.2	+2.8	5
	L90M	−20.2 ± 3.8	−64.1 ± 3.1	33.6 ± 3.5	−50.7 ± 4.6		
SQV	WT	−29.6 ± 4.7	−71.5 ± 4.0	34.7 ± 3.6	−66.4 ± 5.2	+2.7	3.5
	L90M	−27.9 ± 4.2	−72.9 ± 3.8	37.1 ± 3.6	−63.7 ± 4.7		
LPV	WT	−31.2 ± 4.8	−71.1 ± 3.7	41.0 ± 3.4	−61.8 ± 4.5	−0.3	~1
	L90M	−29.8 ± 5.2	−74.1 ± 3.2	41.9 ± 3.4	−62.1 ± 4.9		
PRRT	WT	−74.7 ± 9.3	−84.1 ± 4.2	91.7 ± 5.3	−67.2 ± 7.5	−0.5	-
	L90M	−72.4 ± 6.3	−84.7 ± 4.7	89.4 ± 4.7	−67.7 ± 5.4		

[a] Energy is presented in units of kcal/mol. [b] $T\Delta S$ is not included. [c] $\Delta\Delta G_b = \Delta G_b(\text{L90M}) - \Delta G_b(\text{WT})$ [d] Resistance level was taken from refs 7, 18, and 35. Resistance level is defined as IC90(L90M)/IC90(WT) or as IC50(L90M)/IC50(WT) in the references.

D, hydrogen H, and acceptor A atoms with a D−H···A configuration was regarded as a hydrogen bond when the distance between donor D and acceptor A was shorter than R_{max}(= 3.5 Å) and the angle H−D−A was smaller than Θ_{max}(= 60.0°).

Results

Binding Energy Calculations. The influence of L90M mutation on binding energy ΔGb was examined for each ligand. Table 1 shows the results of MM/PBSA calculations for the WT and L90M PR in complex with each ligand. L90M reduced the binding energies of NFV and SQV. Results of some experiments have suggested that L90M mutation caused resistance against these inhibitors.[7,11−18] On the other hand, L90M PR exhibits almost the same affinity as that of WT PR for LPV. It has been reported that the affinity of LPV was hardly affected by any single mutations.[35] Hence, the results of our simulations are compatible with the results of previous experimental analyses. The affinity of L90 M PR with PRRT is almost the same as that of WT PR.

Hydrogen Bonds between PR and Ligands. Hydrogen bonds play an essential role in stabilizing protein−ligand complexes. We examined 1000 snapshots during the last 500 ps and identified direct or one water molecule-mediated hydrogen bonds (Supporting Information Table S2). NFV mainly creates hydrogen bonds with D25′ and D30 in the WT model. In contrast, NFV interacts with D25 and D25′ in L90M PR. That is, NFV hardly interacts with D30 in the L90M model. It is known that D30 contributes significantly to PR−NFV binding and that the mutation D30N causes specific resistance against NFV.[7,14,57,58] Moreover, in WT and L90M PR, one water molecule is located between I50/I50′ and NFV. This water molecule creates hydrogen bonds with I50′ of WT PR (99.8% of the bonds being maintained during the last 500 ps of simulation) and with I50 of L90M PR (92.4%), while these hydrogen bonds are often broken with NFV in each model (~50%). SQV has a direct interaction with D25′ and a one water molecule-mediated interaction with I50′ in both WT and L90M models. In addition, the main chain at the P2 subsite of SQV makes a hydrogen bond with G48 in both models. In contrast, the side chain at the P2 subsite ($-CONH_2$) interacts with different residues in the two models. The side chain interacts with G48 in the WT model and with D30 in the L90M model. Interestingly, G48 is a residue whose mutation causes specific resistance against SQV.[15−18] Thus, both NFV and SQV lose significant hydrogen bonds due to L90M mutation. On the other hand, LPV has similar hydrogen bond networks in the WT and L90M models. LPV creates direct hydrogen bonds with D25, D25′, and D29. One water molecule connects LPV to the 50th residues by hydrogen bonding. PRRT has similar interactions with D29, D30, and G48 in S4−S1 pockets in the WT and L90M models. However, PRRT has different interactions in S1′-S4′ pockets. One water molecule also stays between D25/D25′ and PRRT in the PR model, while it hardly makes any stable hydrogen bond.

Comparison of the Structures of the WT and L90M Models. To clarify the effect of mutation at the 90th residue on active site conformation, the average structure of the L90M model for the last 500 ps was compared with that of the corresponding WT model. The L90M model was fitted to the WT model using the coordinates of the main chain atoms N, Cα, and C, and the root-mean-squared deviation (RMSD) value was calculated (Figure 2). When the structures of each ligand in the WT and L90M models were compared, some atoms of NFV and SQV were found to exhibit large RMSD values (>2.0 Å). Atoms at the thio-phenol group ($-S-C_6H_5$) in NFV are dislocated to a quite different position, and all of the atoms in SQV are shifted in the same direction. On the other hand, no atoms in LPV exhibit such large RMSD values. In the case of PRRT, the P4−P1′ subsites have almost identical conformations, but there is a prominent difference at the P2′-P4′ subsite. The tertiary structures of the WT PR and L90M PR were also compared. RMSD 3D plots clearly indicate that deviation in the NFV complex model is markedly large compared to other ligand-bound cases. In the case of NFV, main chain atoms at the flap and at P79′ and its neighboring residues show large differences in WT PR and L90M PR. We previously reported conformational changes at the same residues.[33] There are small differences between the results of the present study and those of the previous study regarding the residues at the flap region. Namely, the flap region shows larger deviation from the WT in the present calculation. This is because the residues are flexible (Supporting Information Figure S2) and we examined larger sets of coordinates in this study (1000 sets of coordinates from 1 to 1.5 ns) than the previous study (200 sets of coordinates from 0.9 to 1.0 ns). L90M PR in complex with SQV shows local conformational changes at P81 and its neighbors. In the case of LPV, the main chain atoms at the active site are hardly affected by L90M mutation, although some atoms at the nonactive site show large deviations. In the case of PRRT, the main chain atoms at I50′ and its neighbors show noticeable deviations.

Mechanism of Conformational Changes at the Active Site. Figure 2 shows that L90M mutation affects the location of the

(57) Sugiura, W.; et al. *Antimicrob. Agents Chemother.* **2002**, *46*, 708.
(58) Sugiura, W.; et al. *Jpn. J. Infect. Dis.* **1999**, *52*, 175.

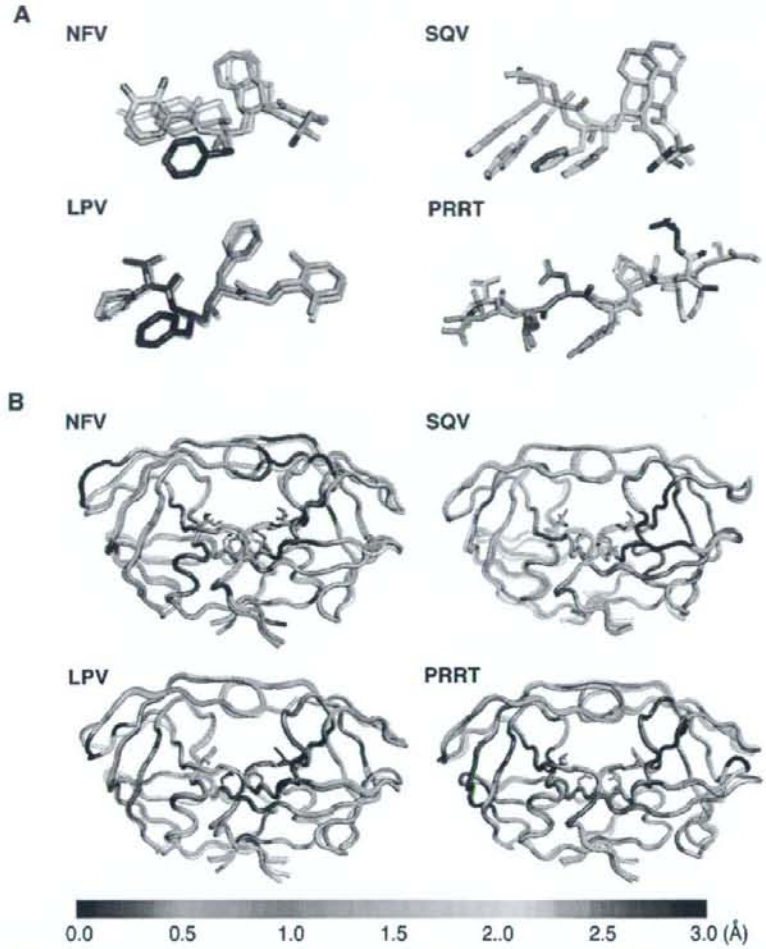

Figure 2. 3D plots of RMSD between the average structures of WT and L90M models. **A**: Ligands in the L90M model are shown as colored sticks. **B**: PRs in the L90M model are shown in colored tube representation, and D25/D25′ and I84/I84′ are shown in stick representation. The color means the magnitude of RMSD shown in the bottom bar. The L90M model was fitted on the WT model using the coordinates of main chain atoms N, Cα, and C of PR. The superimposed gray sticks and tubes represent the structure of the WT model.

ligand and the tertiary conformation of the active site of PR. To determine the reason for induction of these conformational changes at the active site by the nonactive site mutation L90M, conformations of the catalytic triad D25T26G27/D25′T26′G27′ have been examined in detail. These residues have van der Waals contacts with the side chains of the 90th residues[20,26,33] and are located at the active site. In NFV, SQV, and PRRT complex models, some residues showed about 1.0 Å deviations between WT and L90M PR (Supporting Information Table S3). On the other hand, the deviations of all of these residues in the LPV complex model are about 0.5 Å. These residues are the least fluctuating residues in PR because they create rigid hydrogen bond networks, so-called fireman grips[59] (Supporting Information Fig. S2). The root-mean-squared fluctuations (RMSF) of these residues were about 0.3 Å. Thus, these

Table 2. Distances between D25 Cβ-D25′ Cβ, D25 Cβ-I84 Cβ, and 25′ Cβ-I84′ Cβ[a]

D25Cβ-D25′Cβ	NFV	SQV	LPV	PRRT
WT	6.2 ± 0.1	6.7 ± 0.2	7.1 ± 0.2	7.3 ± 0.3
L90M	6.5 ± 0.2	6.2 ± 0.1	7.0 ± 0.2	7.6 ± 0.2
Δ[b]	0.3	−0.5	0.1	0.3
D25Cβ-I84Cβ	NFV	SQV	LPV	PRRT
WT	5.6 ± 0.2	5.0 ± 0.2	4.7 ± 0.2	4.4 ± 0.3
L90M	5.0 ± 0.3	5.1 ± 0.2	4.9 ± 0.2	4.4 ± 0.3
Δ[b]	−0.6	0.1	0.2	0.0
D25′Cβ-I84′Cβ	NFV	SQV	LPV	PRRT
WT	4.4 ± 0.2	5.4 ± 0.4	5.2 ± 0.2	5.0 ± 0.2
L90M	5.8 ± 0.3	5.8 ± 0.2	5.2 ± 0.2	5.1 ± 0.2
Δ[b]	1.4	0.4	0.0	0.1

[a] Distances are presented in units of Å. [b] Difference between L90 M and WT.

conformational changes at these triads are critically important. In the case of NFV, SQV, and PRRT complex models, D25 Cβ -D25′ Cβ distances are also different between the WT and

(59) Strisovsky, K.; Tessmer, U.; Langner, J.; Konvalinka, J.; Kräusslich, H.-G. *Protein Sci.* **2000**, *9*, 1631.

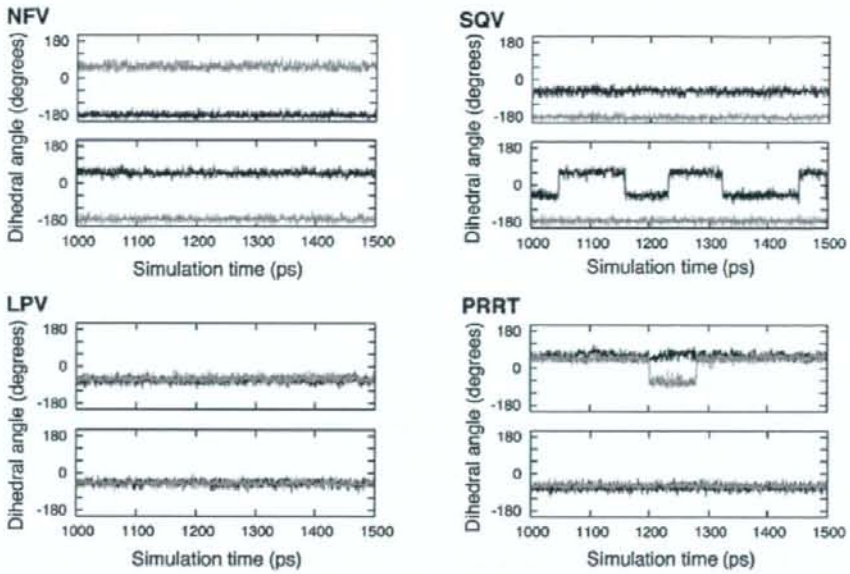

Figure 3. Dihedral angles of N−Cα−Cβ−Cγ1 of I84 (upper) and I84′ (lower) during the last 500 ps of simulations. Red lines represent the WT model, and green lines represent the L90M model.

L90M models (Table 2). There is a particularly large difference in orientations of the side chains of D25/D25′. Furthermore, in the case of NFV and SQV, rotations occur at the side chains of I84/I84′, which are active site residues and are in contact with the side chains of D25/D25′ (Figure 3). The rotations are correlated with the changes in distances between D25 Cβ and I84 Cβ and between D25′ Cβ and I84′ Cβ. That is, the rotations are induced by displacements of the catalytic aspartates D25 and D25′. The side chains of I84/I84′ have large hydrophobic contacts with the ligands, and the structure of the active site is deformed asymmetrically. Consequently, we speculate that the following mechanism causes the active site conformational changes. First, L90M mutation changes the interaction between the 90th residues and D25/D25′. Second, D25/D25′ is shifted. Third, I84/I84′ show rotations of their side chains. Finally, the interaction between ligands and I84/I84′ causes conformational changes of the active site.

Discussion

In HIV-1 PR, the 90th residue is located at the dimer interface, that is, out of the substrate-binding pocket. Hence, it has no direct contact with any ligand of PR. Despite its location, L90M mutation causes resistance against FDA-approved PIs, such as NFV and SQV.[7,11−18] It is difficult to imagine the mechanism of resistance due to L90M mutation. Several X-ray crystal structures have ever been provided for L90M PR.[20−22,26] These structures showed that the side chains of the mutated M90/M90′ altered the interactions with the catalytic aspartates D25/D25′. Hong et al. determined the crystal structure of G48V/L90M HIV-1 PR in complex with SQV. They proposed that alteration in the interactions between the 90th residues and D25/D25′ led to reduction of structural flexibility at the main chains of the catalytic triads and lowered the possibility of these main chains making structural adjustments to SQV.[20] Mahalingam et al. determined the structure of L90M HIV-1 PR in complex with IDV and with substrate analogue inhibitors. They further analyzed kinetic characteristics of L90M mutants and reported that L90M appeared to indirectly lower the dimer stability.[21,22,26] Our recent study in which computational simulations of HIV-1 PR in complex with NFV were carried out suggested that L90M mutation caused a decrease of binding energies and that conformational changes appeared at the flap and 80's loop regions, which are distant from the 90th residues.[33] Hence, for NFV, we concluded that the drug resistance due to L90M was caused by these active site conformational changes. Despite the accumulation of these experimental and theoretical findings, there has been no clear suggestion for drug designs to reduce the degree of or prevent the drug resistance due to L90M.

In this study, investigations of L90M PR were carried out for the purpose of establishing a strategy for promising drug design, and the structures of L90M PR in complexes with NFV, SQV, LPV, and a substrate at the PR/RT cleavage site (PRRT) were analyzed in detail. NFV and SQV lose their inhibitory efficacy for L90M mutation.[7,14−18] In contrast, LPV hardly changes its affinity with PR despite the L90M mutation.[35] The substrate PRRT has a unique sequence, Phe-Pro, at P1/P1′ subunits, whose structure is the basis for the drug design for NFV, SQV, and other PIs.[3,42] In all computed models, changes in interaction between catalytic aspartates D25/D25′ and the 90th residues occur due to the L90M mutation. In contrast, different responses have been observed at the active site of PR in the models. In the L90M PR/NFV complex, L90M causes large conformational changes at the active site, especially at the flap and 80's loop regions of PR. The L90M mutation also causes dislocations of side chains of D25/D25′ and rotations of side chains of I84/I84′. In the L90M PR/SQV complex, a positional shift of SQV and local conformational change at 80's loop

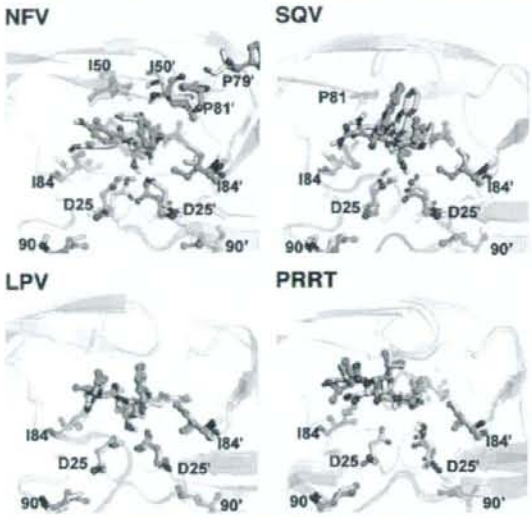

Figure 4. Structure around the active site. Each PR in the L90M model is shown in green cartoon, and each of the ligands and important residues is shown in green ball-and-stick representation. The superimposed gray cartoons and sticks represent the structure of the WT model.

regions occur. Dislocations of the side chains of D25/D25′ and rotations of I84/I84′ also occur, as in the L90M PR/NFV complex. These conformational changes have also been observed in the crystal structure of G48V/L90M PR/SQV complex (PDB code: 1FB7[20]) when compared with WT PR/SQV complex (PDB code: 1HXB[42,49]). In addition, a comparison of the structure of L90M PR in complex with SQV and the crystal structure of G48V/L90M PR/SQV complex shows that the 80's loop, where L90M causes conformational changes, is located at similar positions in the two structures (Supporting Information Figure S3). In the complex with each of these two inhibitors, L90M mutation induces common effects: dislocations of the 25th residues and rotations of the side chains of the 84th residues. In addition, L90M PR decreases the binding energy with each of NFV and SQV, which would reflect the positional shift of the inhibitors. In contrast, in the L90M PR/LPV complex, conformational changes hardly occur at the active site. Dislocations of the 25th residues and rotations of the side chains of the 84th residues hardly appear. Energetically, LPV exhibits the same binding affinity with L90M and WT PRs. PRRT also exhibits the same affinity with L90M and WT PRs, although conformations at both of the residues near I50/I50′ and P2′-P4′ subunits of PRRT are greatly changed. In the PRRT model, no rotation of the side chains of 84I/84′I occurs, while the distance between the two side chains of D25 and D25′ is changed. These results indicate that rotations of the side chains of I84/I84′ are involved in the resistance due to L90M. Consequently, we can conclude that the mechanism of resistance due to L90M is rotations of the side chains of the 84th residues due to dislocations of the side chains of the 25th residues, which are initiated by changes in the interactions between the 90th and the 25th residues. These rotations change the shapes of the active sites, and the change decreases the interactions between PR and ligands (Figure 4). There is still the question of why rotation of the 84th side chains occurs when L90M PR is bound with NFV or SQV but does not occur when L90M PR is bound with LPV and PRRT. The answer to this question is that the rotations is due to not only to dislocations of side chains of D25/D25′ but also to the geometry of the ligand. The shift in side chains of 25D/25′D occurs when L90M PR is bound with NFV, SQV, and PRRT. Focusing on the P1/P1′ subsites of those ligands, NFV and SQV each contain a dodecahydroisoquinoline ring, which is a rigid and bulky functional group, and PRRT has a ring of PRO. These rings are located near D25/D25′ and assist the dislocation of the side chains of D25/D25′ because of their rigidity. Moreover, the size of the rings is responsible for the rotation of the side chains of I84/I84′. Rotation of the side chains of the 84th residues occurs when L90M PR is bound with NFV or SQV. In contrast, rotation hardly occurs despite the side chain dislocations of D25/D25′ when L90M PR is bound with PRRT. The ring size of PRRT is smaller than those of NFV and SQV and makes no unfavorable collision with side chains of I84/I84′. Consequently, the size and flexibility of P1/P1′ subsites of the ligand are closely related to the resistance due to L90 M. We speculate that a single L90M mutation has little effect on the binding affinity with a ligand that has a linear group or a small ring at its P1/P1′ subsite.

We further investigated the interactions between the ligands and each amino acid residue of PRs by performing fragment molecular orbital (FMO) calculations.[60] In the FMO scheme, the total system is divided into fragments and calculations are carried out in parallel, which makes it possible to adopt the ab initio MO calculation for a large molecule like a protein. The single point energy of each model was calculated at the FMO–HF/6-31G level using the ABINIT-MP program[61] The model structures were constructed by the following two steps. First, the average structure was calculated on the basis of 1000 coordinates acquired during the last 500 ps of MD simulation. Next, energy minimization was executed on the average structure. One amino acid residue or one inhibitor was set as a single fragment. It was confirmed from the computational results shown in Figure 5 that each of the ligands indeed interacts with the active site residues or their neighboring residues. Notably, LPV and PRRT interact with only several active site residues. That is, the residues they interact with are quite limited compared with those with which NFV and SQV interact. Furthermore, LPV shows no significant difference between its interactions in WT and L90M PRs. LPV has highly specific interactions with D29 and D25′, whose mutations inactivate the function of the PR.[2,62] Figure 5 also indicates that NFV and SQV show noticeable loss of interaction energies with several residues in both the WT and L90M models. In particular, NFV has unfavorable contact with K45, R87, R8′, D29′, and D30′, and SQV has unfavorable contact with D25′ and D29′. In contrast, LPV shows little energetical loss in the interaction with protein residues in both models. Accordingly, we speculate that this specificity and the little energetical loss are also reasons why L90M mutation has little effect on the binding of LPV.

Last, we investigated whether simulations can provide the correct order in terms of potency of the inhibitors. In the

(60) Kitaura, K.; Sawai, T.; Asada, T.; Nakano, T.; Uebayasi, M. *Chem. Phys. Lett.* **1999**, *312*, 319.
(61) Nakano, T.; Kaminuma, T.; Sato, T.; Fukuzawa, K.; Akiyama, Y.; Uebayasi, M.; Kitaura, K. *Chem. Phys. Lett.* **2002**, *351*, 475.
(62) Ishima, R.; Torchia, D. A.; Lynch, S. M.; Gronenborn, A. M.; Louis, J. M. *J. Biol. Chem.* **2003**, *278*, 43311.

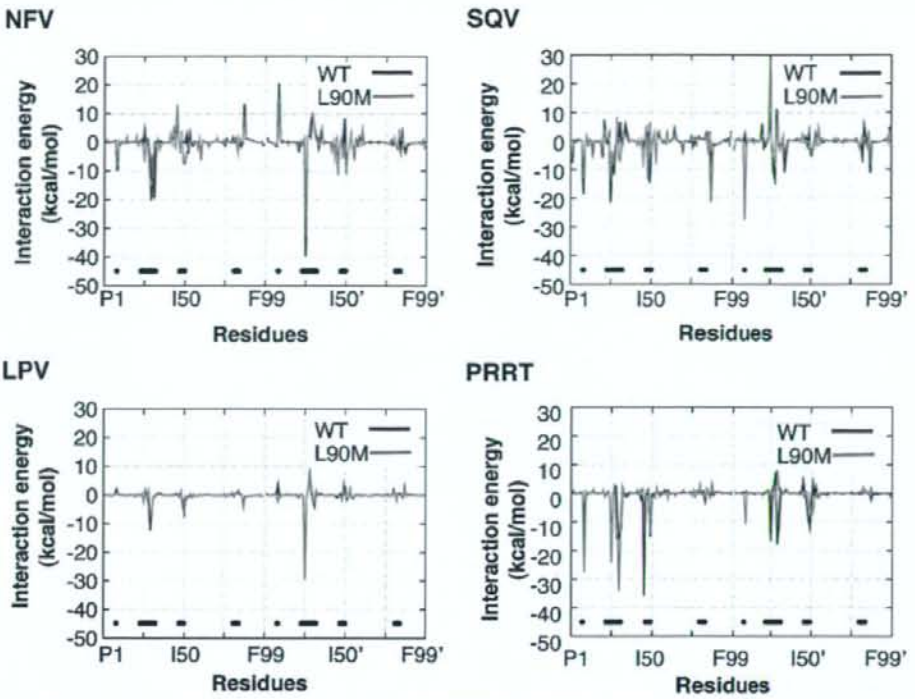

Figure 5. Interresidue interaction energies between PR and ligand calculated by FMO−HF/6-31G. Black lines below indicate the location of the active site residues (R8, L23-V32, I47-I50, P81-I84, R8′, L23′-V32′, I47′-I50′, P81′-I84′).

comparison of ΔG, the calculated inhibitory order for NFV, SQV, and LPV is not compatible with that determined by experiments[63] (Supporting Information Table S4). In contrast, when compared with experimental ΔH, the order in calculated ΔG for the inhibitors is consistent with the experimental measurements. That is because our MM/PBSA calculations do not include entropic terms. Hence, the incorporation of an entropic term will enable us to accurately predict the potency of a new drug by MD simulations.

LPV is one of the most promising drugs for AIDS treatment as shown in the present study. However, as the number of mutations increases, the efficacy of LPV decreases. For example, according to Virologic phenotypic assays, patient-derived HIV-1 confers 20-fold resistance against LPV. The PR sequence of this HIV-1 includes some drug resistant-related mutations (L10I, K20R, M36I, R41K, M46I, F53L, Q61N, L63P, A71V, T74S, V82T, N88S, L90M, I93L). Results of our additional simulation of this resistant PR with LPV have indicated a decrease in inhibitory efficacy ($\Delta G_b = -59.5$ kcal/mol, $\Delta\Delta G_b = +2.3$ kcal/mol) (Supporting Information Figure S4). These mutations decrease the number of hydrogen bonds between LPV and this clinically derived PR (Supporting Information Table S5). Furthermore, the mutations change the conformations at the flap and 80's loop regions (Supporting Information Figure S5). A design to remove the collisions at these regions will further enhance the efficacy of LPV. It should be emphasized that most of the mutated residues are located at the nonactive site of PR. Thus, to create more potent drugs, it is important to clarify the roles of the drug-resistant related nonactive site residues.

On the basis of the findings obtained in this study, we suggest the following strategy for the design of HIV-1 PR inhibitors. First, inhibitors should not contain a large ring such as a dodecahydroisoquinoline ring at P1/P1′ subsites; a linear chemical group is favorable. Second, to remove the collisions at the 80's loop and the flap region, functional groups at P2P1/P1′P2′ subsites of inhibitors should be in the same size as those of PRRT. Third, inhibitors should interact only with limited PR residues such as D25/D25′ and D29/D29′. Finally, inhibitors should not make unnecessary contact with any residues even in WT PR.

In summary, the mechanism of resistance due to the nonactive site mutation L90M has been clarified through theoretical calculations. The 90th residue of HIV-1 PR is located at the dimer interface and has no direct contact with ligand chemicals. The simulations demonstrate that the nonactive site mutation affects conformation of the binding cavity and ligand-binding affinity at the active site. The results of the present study have revealed the drug resistance mechanism of nonactive site mutation and provide a clue for designing a promising drug to reduce the drug resistance due to nonactive site mutation. Adaptive drugs,[64−67] which have the ability to inhibit several variants of a targeting enzyme, are needed in anti-HIV therapy.

(63) Yanchunas, J., Jr.; Langley, D. R.; Tao, L.; Rose, R. E.; Friborg, J.; Colonno, R. J.; Doyle, M. L. *Antimicrob. Agents Chemother.* **2005**, *49*, 3825.

(64) Velazquez-Compoy, A.; Freire, E. *J. Cell. Biochem.* **2001**, *S37*, 82.
(65) Freire, E. *Nat. Biotechnol.* **2002**, *20*, 25.
(66) Ohtaka, H.; Schon, A.; Freire, E. *Biochemistry* **2003**, *42*, 13659.
(67) Ohtaka, H.; Freire, E. *Prog. Biophys. Mol. Biol.* **2005**, *88*, 193.

Some reviews have suggested strategies for the design of adaptive inhibitors for HIV-1 PR.[64,66-69] These strategies, however, do not give sufficient consideration to the structural effects due to nonactive site mutations. The findings of this work should be useful for producing practical adaptive drugs.

Acknowledgment. This work was supported by a Health and Labor Science Research Grant for Research on HIV/AIDS from the Ministry of Health and Labor of Japan and by JSPS Research Fellowships for Young Scientists and a grant-in-aid for JSPS Fellows. A part of this work was also supported by a grant from the Japan Science and Technology Agency.

(68) King, N. M.; Prabu-Jeyabalan, M.; Nalivaika, E. A.; Schiffer, C. A. *Chem. Biol.* **2004**, *11*, 1333.
(69) Prabu-Jeyabalan, M.; Nalivaika, E. A.; Schiffer, C. A. *Structure* **2002**, *10*, 369.

Supporting Information Available: RMSD plots during MD simulations, determination of protonation states of catalytic aspartates in the SQV and/or LPV complex models, a list of hydrogen bond networks in each model, RMSF plot of main chain atoms N, Cα and C in each model, a list of differences between RMSD values (Å) of the main chain atoms in WT and L90M models, comparison of the computed L90M model and the crystal structure (1FG7), comparison of computed ΔG with experimental ΔG and ΔH, results of analyses of the MD simulations of clinically derived HIV-1 PR in complex with LPV, and a complete list of author citations with more than 10 authors. This material is available free of charge via the Internet at http://pubs.acs.org.

JA060682B

Research Letters

AIDS 2008, **22**:1081–1089

Cyclin K/CPR4 inhibits primate lentiviral replication by inactivating Tat/positive transcription elongation factor b-dependent long terminal repeat transcription

Emiko Urano[a,b], Saki Shimizu[a], Yuko Futahashi[a], Makiko Hamatake[a], Yuko Morikawa[b], Naoko Takahashi[c], Hidesuke Fukazawa[c], Naoki Yamamoto[a] and Jun Komano[a]

The positive transcription elongation factor b complexes comprise CDK9 and a C-type cyclin, required for the efficient expression of both eukaryotic and primate lentivirus-encoded genes. Cyclin K/CPR4 is the least studied of the positive transcription elongation factor b-forming cyclins. Here, we demonstrate that cyclin K/CPR4-containing positive transcription elongation factor b complexes are unresponsive to Tat and HEXIM1-mediated inactivation. Enhancing expression of cyclin K/CPR4 inhibited the human and simian immunodeficiency viral replication. These data indicate that cyclin K/CPR4 functions as a natural inhibitor of primate lentiviruses.

Positive transcription elongation factor b (P-TEFb) complexes comprise CDK9 and a C-type cyclin (cyclin T1, T2 or K) and play a role in transcriptional initiation in/or elongation of cellular genes [1–6]. The P-TEFb complex is critical for Tat-dependent transcription from the human and simian immunodeficiency virus (HIV-1 and SIV) long terminal repeat (LTR) promoter. By interacting with the P-TEFb complex, Tat recruits the P-TEFb complex to the trans-activation-responsive (TAR) viral RNA element, which is located close to the transcriptional start site to which Tat binds in complex with P-TEFb complex. CDK9 phosphorylates the carboxy-terminal domain of RNA polymerase II, which boosts transcription from the proviral genome [7]. Among the P-TEFb complex-forming cyclins, only CCNT1 has the Tat responsive motif (TRM). Given the structural and functional similarities between CCNT2 and CCNK [8], expression of CCNK has been assumed to negatively affect Tat-dependent transcription, thus primate lentiviral replication. This possibility, however, has not yet been examined. Recently, it was found that the P-TEFb complex containing CCNT1 or CCNT2 is inactivated by the 7SK RNA–HEXIM1 complex [9–12]. The HEXIM1-mediated inhibition of CCNK-containing P-TEFb complexes remains to be tested.

We constructed mammalian expression plasmids for wild type and N-terminal FLAG-tagged or green fluorescent protein (GFP)-tagged human CCNK (WT, fCCNK or GFP-fCCNK). The CCNK function is unaffected by N-terminal epitope tagging [2,13,14]. GFP-fCCNK was used to examine the intracellular localization of fCCNK in NP2 cells. GFP-fCCNK accumulated in the discrete nuclear speckle compartments, similar to GFP-CCNT1, known to be sites of RNA Pol II-mediated transcription and co-transcriptional premRNA processing [15] and exhibited co-distribution with hemaglutinin eipope tagged CDK9 (data not shown). These data suggest functional similarities between CCNK and CCNT1.

We examined the physical association between CCNK and the transcriptional regulators HEXIM1 and HIV-1 Tat. Under the same conditions, endogenously expressed HEXIM1 did not co-immunoprecipitate with fCCNK, but co-immunoprecipitated successfully with FLAG-tagged CCNT1 (fCCNT1; Fig. 1a). Similarly, FLAG-tagged Tat could not co-immunoprecipitate CCNK under conditions in which it did precipitate GFP-CCNT1 (Fig. 1a). These data suggest that the CCNK-containing P-TEFb complex is unresponsive to HEXIM1 or Tat and, thus, it would appear that CCNK is unique among P-TEFb complex-forming cyclins.

To test whether CCNK expression reduces HIV-1 production at the level of transcription, we performed a transient transfection assay to measure HIV-1 production in the presence of different levels of CCNK expression. HIV-1 proviral DNA was co-introduced into 293 T cells with increasing amounts of fCCNK expression plasmid. It was found that the viral production was decreased dramatically in a dose-dependent manner (Fig. 1b). Similarly, the production of SIV was reduced (data not shown). Western blot analysis revealed that the level of p24 antigen in cell lysates dropped significantly with increasing levels of fCCNK (Fig. 1b). By contrast, the level of the internal control Bip was unaffected (Fig. 1b). Real-time (RT)-PCR analysis revealed that viral mRNA levels fell with increasing fCCNK expression, whereas the internal control cyclophilin A mRNA levels were unaffected (Fig. 1b). The reduction in viral mRNA was comparable with that observed for viral protein. Specifically, RT-PCR demonstrated that 80 ng of pfCCNK exerted the maximum reduction in viral mRNA levels (5.1% relative to the control), a finding similar to the viral production levels quantified by enzyme-linked immunosorbent assay (3.3%, Fig. 1b). These data strongly suggest that CCNK inhibits HIV-1

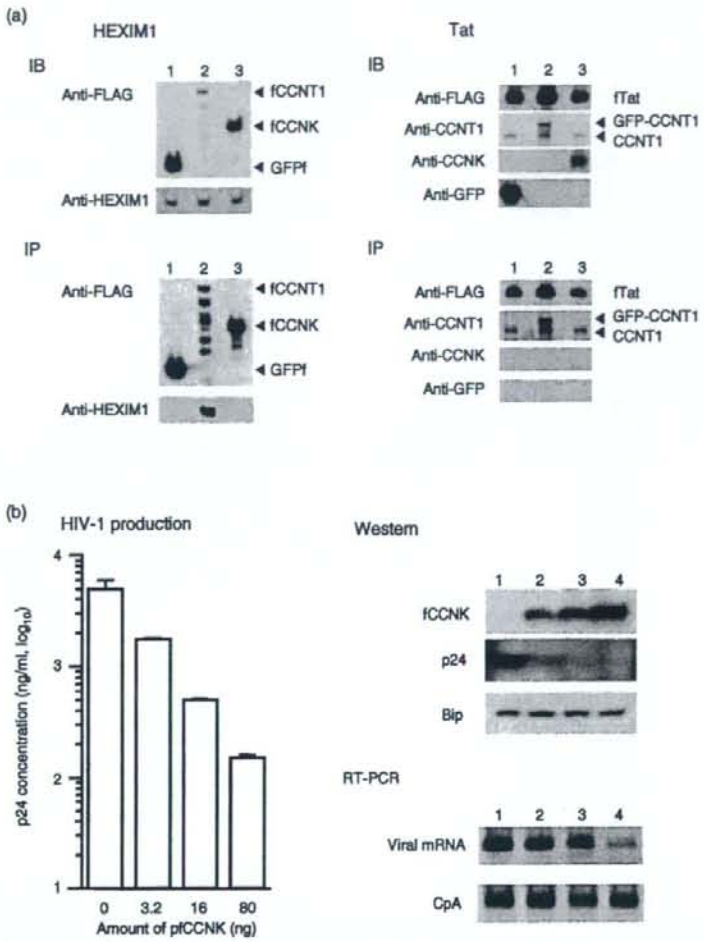

Fig. 1. Expression and functional characterization of cyclin K/CPR4. (a) Co-immunoprecipitation assay demonstrating that cyclin K/CPR4 does not interact with HEXIM1 or HIV-1 Tat. For the co-immunoprecipitation assay with HEXIM1, 293 T cells were transfected with 2 μg of expression vector and then grown in six-well plates. Expression vectors included FLAG-tagged green fluorescent protein (GFP) (lane 1, GFPf), FLAG-tagged CCNT1 (lane 2, fCCNT1) and FLAG-tagged cyclin K/CPR4 (lane 3, fCCNK). For the co-immunoprecipitation assay with Tat, 293 T cells were co-transfected with 1 μg FLAG-tagged Tat (fTat) and 1 μg of GFP (lane 1), GFP-CCNT1 (lane 2) or cyclin K/CPR4 (lane 3). Protein expressions from transfected plasmids were detected by western blot analysis (IB). Cell lysates were immunoprecipitated with agarose beads conjugated with anti-FLAG M2 antibody. Co-immunoprecipitated proteins were separated by SDS-PAGE and immunoblotted using the antibodies indicated (IP). (b) fCCNK expression inhibited transcription of HIV-1. The 293 T cells were co-transfected with HIV-1 proviral DNA (200 ng) and increasing amounts of the fCCNK expression plasmid (0, 3.2, 16 and 80 ng per well in a six-well plate). Viral production was examined 48 h post-transfection by p24 enzyme-linked immunosorbent assay. Western blot analysis was used to examine expression levels of fCCNK, p24 antigen and Bip in transfected 293 T cells. Real-time polymerase chain reaction was used to examine viral and cyclophilin A mRNA expression in transfected 293 T cells. Lanes 1–4 correspond to the amount of pfCCNK 0, 3.2, 16, and 80 ng, respectively.

production by specifically limiting Tat-dependent LTR transcription.

Finally, we investigated the potential inhibitory activity of CCNK on HIV-1 replication in a physiologically relevant system. We established human T cell lines that constitutively overexpressed fCCNK or luciferase (Luc) by infecting MOLT-4, MT-4 and M8166 cells with murine leukemia viral vectors carrying fCCNK-IRES-GFP or Luc-IRES-GFP cassettes and GFP-positive cells were collected as described previously to examine the role of HEXIM1 in the primate lentiviral replication [16]. Expression of fCCNK was verified by western blot analysis using an anti-CCNK antibody and the expression

of cellular proteins such as CCNT1, CDK9, HEXIM1, Bip, and cell surface receptors for HIV-1 (CD4 and CXCR4) was comparable between fCCNK-expressing and Luc-expressing cells. In addition, no differences in rate of cell proliferation were detected between fCCNK-expressing and Luc-expressing cells (data not shown). We measured HIV-1 and SIV replication in these T cell lines and found that the viral replication was strongly inhibited in all the three fCCNK-expressing T cell lines (data not shown). These data directly demonstrate that CCNK functions as a negative regulator of primate lentiviral replication. In addition, we verified that constitutive fCCNK expression did not block the early phase of the viral life cycle by conducting a real-time Alu-LTR PCR assay to quantify the integrated viral genome in MOLT-4 and MT-4 cells infected with VSV-G-pseudotyped replication-incompetent HIV-1 vector (data not shown).

Taken together, our results indicate that CCNK is able to limit the replication of primate lentiviruses by competing with CCNT1 for CDK9, which results in a reduction of CCNT1-containing Tat-responsive P-TEFb complexes, thereby inactivation of Tat/P-TEFb-dependent transcription of the viral LTR promoter. Our report is the first demonstration that constitutive upregulation of a C-type cyclin CCNK limits primate lentiviral replication in human T cell lines without conferring any detectable effect on cell proliferation. The lack of any detectable effect on cell proliferation could be because CCNK-containing P-TEFb complexes can complement the role played by the CCNT1-containing P-TEFb complex in cellular gene transcription. These data highlight the importance of Tat-dependent LTR transcription for the efficient propagation of the primate lentivirus and the potential protective role of CCNK in the pathogenesis of primate lentiviruses.

Acknowledgements

This work was supported in part by the Japan Health Science Foundation, the Japanese Ministry of Health, Labor and Welfare (H18-AIDS-W-003) and the Japanese Ministry of Education, Culture, Sports, Science and Technology (18689014 and 18659136).

[a]AIDS Research Center, National Institute of Infectious Diseases, Shinjuku-ku, Tokyo; [b]Kitasato Institute of Life Sciences, Kitasato University, Minato-ku, Tokyo; and [c]Department of Bioactive Molecules, National Institute of Infectious Diseases, 1-23-1, Toyama, Shinjuku-ku, Tokyo, Japan.

Correspondence to Jun Komano, AIDS Research Center, National Institute of Infectious Diseases, 1-23-1 Toyama, Shinjuku, Tokyo 162-8640, Japan.
Tel: +81 3 5285 1111; fax: +81 3 5285 5037;
e-mail: ajkomano@nih.go.jp

References

1. Peng J, Zhu Y, Milton JT, Price DH. **Identification of multiple cyclin subunits of human P-TEFb.** *Genes Dev* 1998; **12**:755–762.
2. Fu TJ, Peng J, Lee G, Price DH, Flores O. **Cyclin K functions as a CDK9 regulatory subunit and participates in RNA polymerase II transcription.** *J Biol Chem* 1999; **274**:34527–34530.
3. Price DH. **P-TEFb, a cyclin-dependent kinase controlling elongation by RNA polymerase II.** *Mol Cell Biol* 2000; **20**:2629–2634.
4. Garriga J, Grana X. **Cellular control of gene expression by T-type cyclin/CDK9 complexes.** *Gene* 2004; **337**:15–23.
5. Dulac C, Michels A, Fraldi A, Bonnet F, Nguyen Vt, Napolitano GETA. **Transcription-dependent association of multiple positive transcription elongation factor units to a HEXIM multimer.** *J Biol Chem* 2005; **280**:30619–30629.
6. Peterlin BM, Price DH. **Controlling the elongation phase of transcription with P-TEFb.** *Mol Cell* 2006; **23**:297–305.
7. Garber M, Wei P, Jones K. **HIV-1 Tat interacts with cyclin T1 to direct the P-TEFb CTD kinase complex to TAR RNA.** *Cold Spring Harb Symp Quant Biol* 1998; **63**:371–380.
8. Napolitano G, Licciardo P, Gallo P, Majello B, Giordano A, Lania L. **The CDK9-associated cyclins T1 and T2 exert opposite effects on HIV-1 Tat activity.** *AIDS* 1999; **13**:1453–1459.
9. Zhou Q, Yik JH. **The Yin and Yang of P-TEFb regulation: implications for human immunodeficiency virus gene expression and global control of cell growth and differentiation.** *Microbiol Mol Biol Rev* 2006; **70**:646–659.
10. Michels A, Fraldi A, Li Q, Adamson Te, Bonnet F, Nguyen Vt, *et al.* **Binding of the 7SK snRNA turns the HEXIM1 protein into a P-TEFb (CDK9/cyclin T) inhibitor.** *EMBO J* 2004; **23**:2608–2619.
11. Yik J, Chen R, Pezda A, Samford C, Zhou Q. **A human immunodeficiency virus type 1 Tat-like arginine-rich RNA-binding domain is essential for HEXIM1 to inhibit RNA polymerase II transcription through 7SK snRNA-mediated inactivation of P-TEFb.** *Mol Cell Biol* 2004; **24**:5094–5105.
12. Barboric M, Kohoutek J, Price J, Blazek D, Price D, Peterlin B. **Interplay between 7SK snRNA and oppositely charged regions in HEXIM1 direct the inhibition of P-TEFb.** *EMBO J* 2005; **24**:4291–4303.
13. Edwards MC, Wong C, Elledge SJ. **Human cyclin K, a novel RNA polymerase II-associated cyclin possessing both carboxy-terminal domain kinase and Cdk-activating kinase activity.** *Mol Cell Biol* 1998; **18**:4291–4300.
14. Lin X, Taube R, Fujinaga K, Peterlin BM. **P-TEFb containing cyclin K and Cdk9 can activate transcription via RNA.** *J Biol Chem* 2002; **277**:16873–16878; [Epub ahead of print, 1 March 2002].
15. Herrmann CH, Mancini MA. **The Cdk9 and cyclin T subunits of TAK/P-TEFb localize to splicing factor-rich nuclear speckle regions.** *J Cell Sci* 2001; **114**:1491–1503.
16. Shimizu S, Urano E, Futahashi Y, Miyauchi K, Isogai M, Matsuda Z, *et al.* **Inhibiting lentiviral replication by HEXIM1, a cellular negative regulator of the CDK9/cyclin T complex.** *AIDS* 2007; **21**:575–582.

Potential role of CD8+CD28− T lymphocytes in immune activation during HIV-1 infection

Nancy Vivar[a], Pham Hong Thang[a,b], Ann Atlas[c], Francesca Chiodi[a] and Bence Rethi[a,d]

As CD8+CD28− T cells have been associated with dendritic and T cell suppression, we analyzed whether an increase in CD8+CD28− T cell numbers during HIV-1 infection could lead to impaired T cell responses. In contrast to the in-vitro generated CD8+CD28− suppressors, peripheral blood CD8+CD28− T cells of both HIV-infected and

Ligand-independent higher-order multimerization of CXCR4, a G-protein-coupled chemokine receptor involved in targeted metastasis

Makiko Hamatake, Toru Aoki, Yuko Futahashi, Emiko Urano, Naoki Yamamoto and Jun Komano[1]

AIDS Research Center, National Institute of Infectious Diseases, 1-23-1 Toyama, Shinjuku-ku, Tokyo 162-8640, Japan

(Received July 19, 2008/Revised September 1, 2008/Accepted September 7, 2008/Online publication October 31, 2008)

CXCR4, a G-protein-coupled receptor of CXCL12/stromal cell-derived factor-1α, mediates a wide range of physiological and pathological processes, including the targeted metastasis of cancer cells. CXCR4 has been shown to homo-oligomerize in several experimental systems. However, it remains unclear with which domains CXCR4 interacts homotypically, and whether it dimerizes or forms a higher-order complex. To address these issues, we used bioluminescent resonance energy transfer and bimolecular fluorescence complementation analyses to measure the homotypic interactions of CXCR4 in living cells. Both assays indicated that CXCR4 interacts homotypically, which is consistent with previous studies. By studying CXCR4 mutants lacking various domains, we found that multiple transmembrane domains probably serve as potential molecular interaction surfaces for oligomerization. The relative contribution of the amino- or carboxy-termini to oligomerization was small. To differentiate between a dimer and a multimer consisting of more than two molecules, bioluminescent resonance energy transfer–bimolecular fluorescence complementation analysis was conducted. It revealed that CXCR4 engages in higher-order oligomerization in a ligand-independent fashion. This is the first report providing direct experimental evidence for the higher-order multimerization of CXCR4 *in vivo*. We hypothesize that CXCR4 distributes to the cell surface as a multimer, in order to effectively sense, with increased avidity, the chemotaxis-inducing ligand in the microenvironment. Studying the structure and function of the oligomeric state of CXCR4 may lead us to develop novel CXCR4 inhibitors that disassemble the molecular cluster of CXCR4. (*Cancer Sci* 2009; 100: 95–102)

CXCR4, a widely expressed chemokine receptor of CXCL12/stromal cell-derived factor (SDF)-1α, plays a role in various physiological and pathological processes, including neuronal network development, normal and malignant cell migration, inflammatory reactions, the genetic immunodeficiency syndrome WHIM (warts, hypogammaglobulinemia, infections, myelok-athexis), and human immunodeficiency virus (HIV)-1 infection.[1–7] The CXCR4–CXCL12/SDF-1α axis is reportedly involved in the tumor progression of breast cancer and more recently of pancreatic, esophageal, prostate, thyroid, colorectal, and cutaneous cancers.[8–16] Thus, it has been emphasized that the CXCR4–CXCL12/SDF-1α axis may be an important therapeutic target.[9,14] Understanding the regulatory mechanisms of CXCR4 functions may provide clues to develop therapeutic approaches for such disorders.

CXCR4 was shown to homo-oligomerize by several experimental systems. It is possible that CXCR4 dimerizes because CXCL12/SDF-1α forms a dimer, as indicated by structural analyses.[17–19] However, past biophysical analyses did not critically distinguish between dimers and complexes consisting of more than two molecules (the higher-order oligomer).[20–23] The oligomerization of G protein-coupled recepters (GPCR) has been suggested to play a role in ligand-initiated signaling and protein trafficking, including egress from the endoplasmic reticulum (ER) or internalization from the plasma membrane.[24,25] It appears that steady-state oligomerization and its functional significance vary among GPCR species. Although it is known to homo-oligomerize, the functional significance of CXCR4 oligomerization is not well understood. Isolating a monomeric CXCR4 mutant is one straightforward approach toward understanding the functional significance of CXCR4 oligomerization. However, to achieve this goal, it remains to be clarified whether CXCR4 dimerizes or forms a higher-order complex, and with which domains CXCR4 interacts homotypically. Additionally, it is unknown how selfoligomerization is regulated.

It is hypothesized that, for most mammalian GPCR, the stable homotypic interaction is mediated by a specific transmembrane domain (TMD), as has been shown for some GPCR (e.g. dopamine D2 receptor, adenosine A2A receptor, and CCR5).[26–28] If CXCR4 forms a dimer, it is postulated that two CXCR4 molecules should face each other in a symmetrical configuration on the two-dimensional plane of the biological lipid bilayer (Fig. 1a). If this were the case, it might not be difficult to isolate a CXCR4 mutant lacking TMD that fails to interact homotypically. However, if CXCR4 has multiple interaction facets that multimerize, monomeric CXCR4 mutants may be hard to isolate by the simple mutagenesis approach (Fig. 1b).

To measure TMD–TMD interactions, we used bioluminescent resonance energy transfer (BRET) and bimolecular fluorescence complementation (BiFC) assay systems[29,30] that allowed us to measure the specific homotypic and heterotypic interactions of membrane proteins bearing multiple TMD in living mammalian cells. By analyzing a series of CXCR4 mutants using these two techniques, we found that CXCR4 forms a steady-state molecular cluster consisting of more than two molecules, and that this cluster formation is not mediated by the amino- or carboxy-termini. This is the first report to provide direct experimental evidence that CXCR4 engages in higher-order multimerization *in vivo*.

Materials and Methods

Plasmids. The plasmids pCXCR4, pCXCR4-GFP, and d-31-GFP were described previously.[31] The following oligonucleotides encoding the myristoylation and palmitoylation signal region of *lyn* were annealed and cloned into the *Eco*RI and *Bam*HI sites of pDsRed2-N1 (Clontech, Palo Alto, CA, USA), generating pLynDsRed2: sense, 5′-AATTGCCACCATGGGATGTATTAAA-TCAAAAAGGAAAGAC-3′ and antisense, 5′-GATCGTCTTTC-CTTTTTGATTTAATACATCCCATGGTGGC-3′. The *Sna*BI–*Age*I fragment from pLynDsRed2 was cloned into the corresponding sites of pEGFP-C2, generating pMEM-GFP. The 5′ *Nhe*I end of

[1]To whom correspondence should be addressed. E-mail: ajkomano@nih.go.jp

doi: 10.1111/j.1349-7006.2008.00997.x

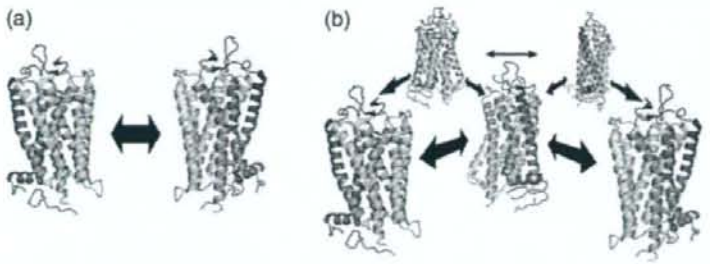

Fig. 1. Hypothetical models of CXCR4 oligomerization. (a) If CXCR4 forms a dimer, it is postulated that two CXCR4 molecules would physically associate with each other via the specific side of the molecule where the same key transmembrane helices are situated. (b) If CXCR4 forms a higher-order multimerization consisting of more than two molecules, CXCR4 should have multiple interaction domains. These models were drawn based on the bovine rhodopsin structure.

the *Nhe*I–*Xba*I fragment from phRL/CMV (Promega, Madison, WI, USA) encoding renilla luciferase (hRL) was ligated to the annealed oligonucleotides of 5′-AGATCTGGTTACCCAATT-3′ and 5′-CTAGAATTGGGTAACCAGATCT-3′. The 3′ end of the same fragment was ligated to the annealed oligonucleotides of 5′-CTAGGATCTGAATTCAGATCT-3′ and 5′-AGATCTGAATTCAGATC-3′. The *Bgl*II fragment was cloned into the *Bgl*II and *Bam*HI sites of pEGFP-C3 (Clontech), generating pEGFP-hRluc. The plasmid pCXCR4 FL-Rluc was constructed by cloning the *Mfe*I fragment from pEGFP-hRLuc BRET into the *Eco*RI and *Mfe*I sites of pCXCR4.

5TMDΔ23 was amplified by a two-step polymerase chain reaction (PCR). In the first step, PCR products were amplified by two separate PCR using the following two primer pairs targeting full-length CXCR4: R4 forward 5′-ACCGGTGCCACCATGGAGGGGATCAGTATATACACTTCAG-3′ and 5TMDΔ23 reverse 5′-GGGATCCAGACGCCAACATAGACCACCTTGTCCGTCATGCTTCTCAGTTTCTTC-3′; 5TMDΔ23 forward 5′-GAAGAAACTGAGAAGCATGACGGACAAGGTGGTCTATGTTGGCGTCTGGATCCC3′ and R4 reverse 5′-AGATCTCGCTGGAGTGAAAACTTGAAGACTCAGACTC-3′. The second PCR step was carried out by mixing the two first-step PCR products and amplifying the DNA with the R4 forward and R4 reverse primers. The final PCR product was cloned into pCRblunt2-TOPO (Invitrogen, Tokyo, Japan) and sequenced. The *Age*I–*Bgl*II fragment, encoding 5TMDΔ23, was cloned into the *Age*I and *Bgl*II sites of pCXCR4-GFP and pCXCR4 FL-Rluc, generating pCXCR4 5TMDΔ23-GFP and pCXCR4 5TMDΔ23-Rluc, respectively. The 5TMDΔ12, 5TMDΔ34, 5TMDΔ34, and 5TMDΔ34 derivatives were generated similarly by using the following primers: 5TMDΔ12 forward 5′-CCGTGAAGAAAATGCTAATTTCAATAAAGCAGTCCATGTCATCTACACAGTTAACCTC-3′, 5TMDΔ12 reverse 5′-GAGGTTAACTGTGTAGATGACATGGACTGCTTTATTGAAATTAGCATTTTCTTCACGG-3′, 5TMDΔ34 forward 5′-CTGGTACTTTGGGAACTTCCTATGCAAGCACATCATGGTTGGCCTTATCCTGCC-3′, 5TMDΔ34 reverse 5′-GGCAGGATAAGGCCAACCATGATGTGCTTGCATAGGAAGTTCCCAAAGTACCAG-3′, 5TMDΔ45 forward 5′-GGCCAAGGAAGCTGTTGGCTGAAAAGACCACAATCATCCCCATCCTGGCTTTC-3′, 5TMDΔ45 reverse 5′-GAAAGCCAGGATGGGGATGATTGTGGTCTTTTCAGCCAACAGCTTCCTTGGCC-3′, 5TMDΔ67 forward 5′-GTCCTGCTATTGCATTATCATCTCCAAATTTAAAACCTCTGCCCAGCACGCACTC-3′, and 5TMDΔ67 reverse 5′-GAGTGCGTGCTGGGCAGAGGTTTTAAATTTGGAGATGATAATGCAATAGCAGGAC-3′. The 3TMD125 and 3TMΔ367 derivatives were constructed by conducting a two-step PCR using the 5TMDΔ34 forward and reverse primers with 5TMDΔ67 and 5TMDΔ12 as templates, respectively.

The plasmid pCXCR4 d-31-Rluc was constructed by replacing the *Age*I–*Bgl*II region of pCXCR4-Rluc with the *Age*I–*Bgl*II fragment from pCXCR4 d-31-GFP. The plasmid pCXCR2/444 has been described previously,[32] and the *Sna*BI–*Bam*HI fragment from pCXCR2/444 replaced the *Sna*BI–*Bam*HI region of pCXCR4-GFP, generating pCXCR2/4-GFP.

The following oligonucleotides encoding the amino-terminal myristoylation signal region of *lyn* were annealed and cloned into the *Eco*RI and *Bam*HI sites of pEGFP-N1, generating pLyn-GFP: sense 5′-AATTGCCACCATGGGAGCTATTAAATCAAAAAGGAAAGAC-3′ and antisense 5′-GATCGTCTTTCCTTTTTGATTTAATAGCTCCCATGGTGGC-3′. The plasmid pLyn-R4cyt-GFP was constructed by cloning the *Xma*I fragment of a PCR product amplified by 5′-CCCGGGGAAATTTAAAACCTCTGCCC-3′ and 5′-CCCGGGCTGGAGTGAAAACTTGAAG-3′ using pCXCR4-GFP as a template into the *Age*I site of pLynGFP.

CXCR3 was amplified from RNA extracted from human peripheral blood mononuclear cells by reverse transcription-PCR using the following primers; 5′-ACCGGTGCCACCATGGTCCTTGAGGTGAGTGACC-3′ and 5′-GAGCTCGAGATCTCCAAGCCCGAGTAGGAGGCCTCTG-3′. CXCR2 was amplified from a plasmid carrying the CXCR2 open reading frame by PCR using the following primers: 5′-GCCACCGGTGCCACCATGGAAGATTTTAACATGG-3′ and 5′-CCTCGAGCCGAGAGTAGTGGAAGTGTGCCCTG-3′. The *Age*I and *Xho*I fragments encoding CXCR2 and CXCR3 were further cloned into the corresponding sites of pCXCR4-GFP and pCXCR4-Rluc, generating pCXCR2-GFP and pCXCR3-GFP, and pCXCR2-Rluc and pCXCR3-Rluc, respectively. The *Bgl*II and *Mfe*I fragments from phmKGN-MN or phmKGC-MN encoding the fragments of Kusabira-Green (mKG) (MBL, Nagoya, Japan) were cloned into the corresponding sites of pCXCR4-GFP, generating pCXCR4-mKGN and pCXCR4-mKGC, respectively. The *Xho*I and *Mfe*I fragments from phmKGN-MN and phmKGC-MN were cloned into the corresponding sites of pCXCR3-GFP, generating pCXCR3-mKGN and pCXCR3-mKGC, respectively.

Cells, transfection, and imaging. All mammalian cells were maintained in RPMI-1640 (Sigma, St Louis, MO, USA) supplemented with 10% fetal bovine serum (Japan Bioserum, Tokyo, Japan), 50 U/mL penicillin, and 50 μg/mL streptomycin (Invitrogen). Cells were incubated at 37°C in a humidified 5% CO_2 atmosphere. Cells were transfected with Lipofectamine 2000 according to the manufacturer's protocol (Invitrogen). Cells were imaged by confocal microscopy as described previously.[31]

Western blotting. Western blotting was carried out according to techniques described previously,[33] except that the cells were processed with an M-PEK kit according to the manufacturer's protocol (Calbiochem, Darmstadt, Germany). The antibodies used are as follows: a monoclonal anti-FLAG epitope (M2; Sigma), a monoclonal anti-GFP antibody (MAB3580; Chemicon International, Temecula, CA, USA), a monoclonal anti-Rluc antibody (MAB4400 and MAB4100; Chemicon), and EnVision+ (Dako, Glostrup, Denmark).

Bioluminescent resonance energy transfer assay. 293T cells grown in a six-well plate were transfected with 0.05–0.2 μg renilla luciferase (Rluc) derivatives along with 1–2 μg of the green fluorescent protein (GFP) fusion derivative expression plasmids. Varying amounts of plasmids were used to control the expression levels of GFP and Rluc in the transfected cells. At 2 days after transfection, cells were collected and incubated with the Rluc

doi: 10.1111/j.1349-7006.2008.00997.x

substrate according to the manufacturer's protocol except that a 10-fold higher substrate concentration was used (ViviRen Live Cell Substrate; Promega). The fluorescent and bioluminescent signals were measured using a Tristar LB941 (Berthold Technologies, Bad Wildbad, Germany).

Bimolecular fluorescence complementation–BRET analysis. 293T cells grown in a six-well plate were cotransfected with equal amounts of mKGN and mKGC (31.3–1000 ng) along with the Rluc constructs for CXCR4 or CXCR3 (20–200 ng). The BiFC–BRET signal was measured according to the BRET protocol described above.

Results

Establishment of the BRET system to measure molecular interactions. We used the BRET system to measure the homotypic interaction of CXCR4 (Fig. 2a). Wild-type CXCR4 was fused to either enhanced GFP or Rluc at its carboxy-terminus. Previous studies indicate that CXCR4 function is not affected by this modification.[31,34,35] The expression of CXCR4-GFP and CXCR4-Rluc were verified by western blot analysis using anti-GFP and anti-Rluc antibodies, confocal microscopy, flow cytometric analysis, and immunofluorescence analysis (Fig. 2b,c; data not shown). Two days after cotransfection of the CXCR4-GFP and CXCR4-Rluc expression plasmids into 293T cells, we incubated cells with the cell-permeable Rluc substrate and measured the GFP fluorescence, the net Rluc bioluminescence, and the bioluminescence through 485-nm (window A) and 525-nm (window B) emission filters. The BRET efficiency was defined as the ratio of the window B and window A values. As a positive control, we used the GFP-Rluc fusion protein that should theoretically have the best BRET efficiency. As a negative control, we cotransfected cells with GFP and Rluc expression plasmids. The average and standard deviation of BRET values between CXCR4-GFP and CXCR4-Rluc was 1.103 ± 0.160 where the negative and positive controls yielded 0.667 ± 0.084 and 1.444 ± 0.109, respectively (Table 1). The CXCR4 BRET signals were significantly higher than those of the negative control ($P < 0.001$, Student's t-test). Even the transfected cells expressed ~5–10-fold higher levels of GFP and Rluc in the negative control than did cells transfected with pCXCR4-GFP and pCXCR4-Rluc (data not shown).

The specificity of CXCR4-to-CXCR4 BRET signals has been a concern, as GPCR may yield non-specific BRET signals. To address this, we carried out out two experiments: a competition assay and a BRET measurement between heterologous chemokine receptors. The tripartite transfection of cells with pCXCR4, pCXCR4-GFP, and pCXCR4-Rluc resulted in a reduction of the BRET signal to 0.812 ± 0.058, which is significantly less than the BRET levels between CXCR4-GFP and CXCR4-Rluc ($P < 0.001$; Table 1). We defined the BRET level between GFP and Rluc as 0%, and that between CXCR4-GFP and CXCR4-Rluc as 100%, and used these normalized values to determine the relative BRET efficiency of each interaction. The presence of pCXCR4 reduced the BRET level to 39.3%, most likely because of the interference of the BRET-inducing homotypic CXCR4 interaction by untagged CXCR4.

We next examined various chemokine receptors, including CXCR2, CXCR3, and CCR5. Membrane targeting of these chemokine receptors was visualized by confocal microscopy (Fig. 2c), fluorescence activated cell sorting (FACS) analysis, and an immunofluorescence assay (data not shown). CXCR4-Rluc yielded low BRET signals (Table 1) with either membrane-targeted GFP (MEM-GFP; 0.609 ± 0.041, 0.0%), CXCR2-GFP (0.791 ± 0.093, 16.4%), CXCR3-GFP (0.718 ± 0.083, 7.9%), or CCR5-GFP (0.737 ± 0.057, 2.0%). Similar observations were made for the BRET signals between CXCR4-GFP and CXCR2-Rluc (0.762 ± 0.093, 10.2%) or CXCR4-GFP and CXCR3-Rluc (0.709 ± 0.064, 6.2%). These data suggest that the BRET assay detects specific homotypic interactions of CXCR4. Consistent with this, we also detected the homotypic interaction of CXCR4, but not the CXCR4–CXCR3 interaction, using a BiFC assay. Although some have suggested a possible homotypic interaction of CXCR2,[36] this interaction did not yield BRET signals as high as those with CXCR4 in our experimental set up, suggesting that the homotypic interaction of CXCR4 is substantially stronger than that of other chemokine receptors. Throughout this study, the BRET and BiFC assays were carried out under conditions where the transfected cells expressed similar levels of GFP and Rluc.

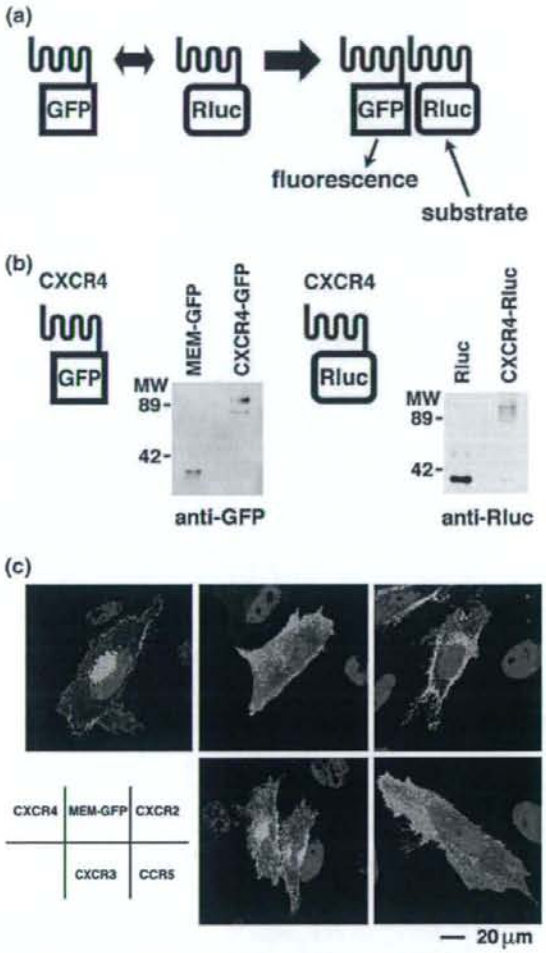

Fig. 2. Bioluminescent resonance energy transfer (BRET) assay to detect CXCR4 homotypic interactions. (a) Schematic drawing of the BRET assay system. The bioluminescence energy from renilla luciferase (Rluc) was absorbed by green fluorescent protein (GFP) to emit green fluorescence. (b) Detection of CXCR4-GFP and CXCR4-Rluc expression by western blotting. The GFP and Rluc fusion proteins were detected by anti-GFP and anti-Rluc antibodies, respectively. The molecular-weight markers are indicated on the left (kDa). (c) The intracellular distribution of CXCR4-GFP (top, left), MEM-GFP (top, middle), CXCR2-GFP (top, right), CXCR3-GFP (bottom, left), and CCR5-GFP (bottom, right). Green and blue represent GFP and the Hoechst 33258-stained nucleus, respectively. Magnification, ×630; scale bar = 20 μm.

Table 1. Detection of specific CXCR4–CXCR4 interactions by bioluminescent resonance energy transfer (BRET) analysis

Sample	BRET level[1]	*n*	*P*-value	Relative BRET efficiency (%)[2]
GFP-Rluc fusion protein	1.444 ± 0.109	20	Not tested	–
GFP + Rluc	0.667 ± 0.084	21	Not tested	0.0
CXCR4-GFP + CXCR4-Rluc	1.103 ± 0.160	21	Not tested	100.0
CXCR4 FL-GFP + CXCR4-Rluc + CXCR4	0.812 ± 0.058	4	<0.001	39.3
MEM-GFP + CXCR4-Rluc	0.609 ± 0.041	5	<0.001	0.0
CXCR2-GFP + CXCR2-Rluc	0.784 ± 0.096	6	<0.001	13.0
CXCR2-GFP + CXCR4-Rluc	0.791 ± 0.093	6	<0.001	16.4
CXCR4-GFP + CXCR2-Rluc	0.762 ± 0.093	6	<0.001	10.2
CXCR3-GFP + CXCR3-Rluc	0.688 ± 0.060	6	<0.001	5.1
CXCR3-GFP + CXCR4-Rluc	0.718 ± 0.083	6	<0.001	7.9
CXCR4-GFP + CXCR3-Rluc	0.709 ± 0.064	6	<0.001	6.2
CCR5-GFP + CXCR4-Rluc	0.737 ± 0.057	4	<0.001	2.0

[1]The average and standard deviation of the indicated number of independent experiments.
The statistical significance of each BRET efficiency was tested compared to the BRET signal of CXCR4-GFP and CXCR4-Rluc (Student's *t*-test).
[2]The relative BRET efficiency for each experiment was averaged.

Fig. 3. Analyses of the transmembrane domain (TMD) mutants of CXCR4. (a) Schematic drawing of CXCR4 5TMD mutants. The deleted portions are indicated in gray. The intracellular distribution of 5TMDΔ23-GFP is shown as a representative. Green and blue represent green fluorescent protein (GFP) and the Hoechst 33258-stained nucleus, respectively. Magnification, ×630; scale bar = 20 μm. (b) Detection of CXCR4 5TMD-GFP and 5TMD-Rluc derivative expression by western blotting. The GFP and renilla luciferase (Rluc) fusion proteins were detected by anti-GFP and anti-Rluc antibodies, respectively.

Measuring the interaction between CXCR4 mutants carrying five TMD. The dimerization model predicts the presence of a CXCR4 mutant defective in the homotypic interaction. To map the domains required for the homotypic interaction of CXCR4, we constructed a series of deletion mutants. It has been reported that removing two transmembrane domains alters neither the membrane topology nor the functions of CXCR4.[37] Thus, we constructed four mutants, 5TMDΔ23, 5TMDΔ34, 5TMDΔ45, and 5TMDΔ67, and fused these mutants to either GFP or Rluc at their carboxy-termini (Fig. 3a). The expression of the 5TMD derivatives was verified by western blot analysis (Fig. 3b). The intracellular distribution of 5TMDD23-GFP was mostly cytoplasmic with reticular patterns (Fig. 3a), and all 5TMD-GFP derivatives showed similar distributions. The BRET efficiencies of homotypic pairs of GFP- and Rluc-tagged 5TMD derivatives were comparable to those of full-length CXCR4 (109.4–133.8%; Table 2). Furthermore, any pair of 5TMD derivatives yielded BRET signal levels similar to those of CXCR4-GFP and CXCR4-Rluc (81.8–161.0%; Table 2). None of the combinations yielded significantly lower BRET signals than the full-length CXCR4

Table 2. Detection of homotypic and heterotypic interactions between five transmembrane domain (5TMD) derivatives by bioluminescent resonance energy transfer (BRET) analysis

Sample	BRET level[1]	*n*	Relative BRET efficiency (%)[2]
Homotypic interaction			
5TMDΔ23-GFP + 5TMDΔ23-Rluc	1.130 ± 0.091	7	115.7
5TMDΔ34-GFP + 5TMDΔ34-Rluc	1.209 ± 0.097	10	133.8
5TMDΔ45-GFP + 5TMDΔ45-Rluc	1.117 ± 0.095	7	112.6
5TMDΔ67-GFP + 5TMDΔ67-Rluc	1.102 ± 0.087	7	109.4
Heterotypic interaction			
5TMDΔ23-GFP + 5TMDΔ34-Rluc	1.060 ± 0.085	4	104.5
5TMDΔ23-GFP + 5TMDΔ45-Rluc	1.078 ± 0.093	3	112.7
5TMDΔ23-GFP + 5TMDΔ67-Rluc	0.978 ± 0.078	7	81.8
5TMDΔ34-GFP + 5TMDΔ23-Rluc	1.299 ± 0.077	3	161.0
5TMDΔ34-GFP + 5TMDΔ45-Rluc	1.177 ± 0.091	3	129.7
5TMDΔ34-GFP + 5TMDΔ67-Rluc	1.225 ± 0.105	3	141.3
5TMDΔ45-GFP + 5TMDΔ23-Rluc	1.080 ± 0.108	8	105.5
5TMDΔ45-GFP + 5TMDΔ34-Rluc	1.131 ± 0.050	4	121.5
5TMDΔ45-GFP + 5TMDΔ67-Rluc	1.161 ± 0.069	3	133.7
5TMDΔ67-GFP + 5TMDΔ23-Rluc	1.072 ± 0.096	3	111.3
5TMDΔ67-GFP + 5TMDΔ34-Rluc	1.065 ± 0.088	4	104.8
5TMDΔ67-GFP + 5TMDΔ45-Rluc	1.042 ± 0.094	3	104.0

[1]The average and standard deviation for the indicated number of independent experiments.
The statistical significance of each BRET efficiency was tested compared to the BRET signal of CXCR4-GFP and CXCR4-Rluc (Student's *t*-test). All were found to be not significant.
[2]The relative BRET efficiency was calculated for each experiment and the average is shown.

combination. These data suggest that either: (1) the interactions between the 5TMD mutants are mediated by the amino- or caroboxy-termini, or the first TMD, as these are shared by all of the 5TMD derivatives; or (2) there are more than two interaction facets in CXCR4, which would make interactions between any two of the 5TMD mutants possible.

Contribution of the amino- or carboxy-terminal domains and the first TMD to CXCR4 oligomerization. To differentiate between the above possibilities, we assessed the potential contribution of the extracellular amino-terminal and the cytoplasmic carboxy-terminal domains to CXCR4 oligomerization. We used a CXCR2–CXCR4 chimeric construct, CXCR2/4, which has the amino-terminus of CXCR2 fused to the first TMD of CXCR4 (Fig. 4a). CXCR2/4 is

doi: 10.1111/j.1349-7006.2008.00997.x

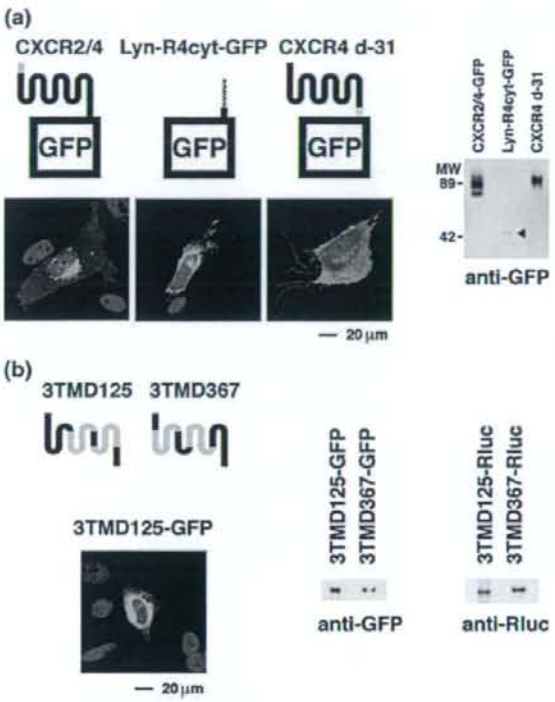

Fig. 4. Assessment of the relative contribution of the CXCR4 amino- and carboxy-termini and the first transmembrane domain (TMD) to oligomerization. (a) Schematic drawing of CXCR2/4-GFP (left), Lyn-R4cyt-GFP (middle), and CXCR4 d-31 (right). The substituted or deleted regions are indicated in gray. The intracellular distribution of each construct is shown. Protein expression was detected by anti-GFP antibody (Lyn-R4cyt-GFP, arrowhead). The molecular-weight markers are indicated on the left (kDa). (b) Schematic drawing of the CXCR4 3TMD mutants. The deleted portions are indicated in gray. The green fluorescent protein (GFP) and renilla luciferase (Rluc) fusion proteins were detected by anti-GFP and anti-Rluc antibodies, respectively. The intracellular distribution of 3TMD125-GFP is shown as a representative. Green and blue represent GFP and the Hoechst 33258-stained nucleus, respectively. Magnification, ×630; scale bar = 20 μm.

known to support HIV-1 entry and CXCL12/SDF-1α signaling.[32,38] The intracellular distribution of CXCR2/4-GFP was similar to that of CXCR4-GFP (Fig. 4a). The interaction between CXCR2/4-GFP and CXCR4-Rluc yielded the BRET signal (to 1.163 ± 0.106, 71.9%; Table 3), which was not significantly different from the BRET levels of CXCR4-GFP and CXCR4-Rluc. Given that only a low BRET signal was detected between CXCR2 and CXCR4 in these experimental conditions (Table 1), this suggests that the amino-terminus of CXCR4 contributes little to its oligomerization.

We next investigated the cytoplasmic tail of CXCR4. The amino-terminus of the CXCR4 cytoplasmic domain was fused to the myristoylation signal motif of *lyn* and the carboxy-terminus was fused to GFP (Lyn-R4cyt-GFP), thereby allowing the cytoplasmic domain of CXCR4 to target the plasma membrane in a native membrane topology (Fig. 4a). As expected, Lyn-R4cyt-GFP was distributed to the plasma membrane, as indicated by microscopic observation (Fig. 4a). However, the BRET signal between Lyn-R4cyt-GFP and CXCR4-Rluc was not detected (0.758 ± 0.057, 4.8%; Table 3). We also tested the cytoplasmic tail-deleted mutant of CXCR4 (Fig. 4a). By removing the cytoplasmic tail of CXCR4, it lost its ability to signal upon ligand binding, but retained its HIV-1 coreceptor function.[32,38] When the carboxy-terminal 31 amino acids were removed (CXCR4 d-31), the BRET signal between CXCR4 d-31-GFP and CXCR4-Rluc was 1.111 ± 0.083 (98.9%), which is comparable to levels seen with the homotypic interaction of full-length CXCR4 (Table 3). These data suggest that CXCR4 oligomerization is not mediated by the amino- or carboxy-termini, but mainly by TMD.

Finally, to examine the possible role of the first TMD in CXCR4 oligomerization, we constructed two CXCR4 mutants carrying three TMD. The 3TMD125 and 3TMD367 mutants have the first, second, and fifth, or the third, sixth, and seventh TMD, respectively, and both were fused to either GFP or Rluc (Fig. 4b). The intracellular distribution of 3TMD-GFP derivatives was similar to those of the 5TMD-GFP derivatives (3TMD125-GFP in Fig. 4b). If the first TMD plays a major role in CXCR4 oligomerization, the BRET signal between 3TMD125-GFP and 3TMD125-Rluc derivatives should be higher than that between 3TMD367 derivatives. Furthermore, if the dimerization model is correct, then the 3TMD125 and 3TMD367 derivatives should not yield detectable BRET signals as they do not share any TMD. We found that the BRET signal representing the homotypic interaction of 3TMD125 was 0.806 ± 0.071 (30.8%), which was significantly higher than the negative control ($P < 0.01$) but lower than that of 3TMD367 (0.917 ± 0.061, 64.0%, $P < 0.05$; Table 3). These data are not consistent with the dimerization model, suggesting that the contribution of the first TMD to the homotypic CXCR4 interaction is relatively small.

The heterotypic interactions between 3TMD and 5TMD derivatives were also tested by the BRET assay. The 3TMD and 5TMD combinations yielded BRET signals that were significantly higher than the 3TMD combinations (72.0 ± 17.5 vs 51.5 ± 16.2%, $P < 0.05$; Table 3) but lower than the 5TMD pairs (72.0 ± 17.5 vs 117.7 ± 18.7%, $P < 0.001$; Tables 2,3). The observations that any pair of 5TMD mutants yielded BRET signals that were comparable to those of CXCR4, and that the BRET signals increased in parallel to the number of TMD, do not agree with a dimerization model and instead favor a multimerization model.

Detecting a higher-order oligomerization of CXCR4 with the BiFC–BRET system. We used the BiFC–BRET technique to directly demonstrate the presence of a trimolecular complex *in vivo*.[39] BiFC uses a 'split' GFP that fluoresces only when the amino- and carboxy-terminal fragments are forced into close proximity. When the BiFC assay is built into the BRET system, the BRET signal should be detected only when three molecules assemble, that is, proteins carrying Rluc and the amino- or carboxy-terminal fragments of GFP (Fig. 5a). We used monomeric mKG as a GFP.[40] The expression vectors of CXCR4 fused to the mKG amino- and carboxy-terminal fragments (mKGN and mKGC, respectively) were constructed. For controls, we constructed CXCR3-mKGN and CXCR3-mKGC. The expression of fusion proteins was verified by immunofluorescence analysis (Fig. 5b) and flow cytometric analysis (data not shown).

We detected BiFC signals when CXCR4-mKGN and CXCR4-mKGC were coexpressed, but not when either was expressed alone or when a pair of CXCR4 and CXCR3 derivatives were coexpressed, confirming the specificity of the BiFC analysis and the BRET results (Fig. 5b; Table 4). We considered the combination of CXCR4-mKGN, CXCR4-mKGC, and Rluc as a negative control. When increasing amounts of pCXCR4-mKGN and pCXCR4-mKGC were transfected into 293T cells along with pCXCR4-hRluc, we detected increasing BiFC–BRET signals that were significantly higher than the negative control (Table 4). Such high BiFC–BRET signals were not observed by tripartite transfection of plasmids expressing CXCR4-mKGN, CXCR4-mKGC, and CXCR3-Rluc, CXCR3-mKGN, CXCR3-mKGC, and CXCR4-Rluc, or CXCR4-mKGN, CXCR4-mKGC, and Rluc

Table 3. Contribution of the amino- and carboxy-terminal domains, and the first transmembrane domain (TMD) to CXCR4 oligomerization as analyzed by bioluminescent resonance energy transfer (BRET) analysis

Sample	BRET level[†]	*n*	*P*-value	Relative BRET efficiency (%)[‡]
Amino- and carboxy-terminal domain				
CXCR2/4-GFP + CXCR4-Rluc	1.163 ± 0.106	6	n.s.	71.9
Lyn My-R4cyt-GFP + CXCR4-Rluc	0.758 ± 0.057	4	<0.001	4.8
CXCR4 d-31-GFP + CXCR4-Rluc	1.111 ± 0.083	8	n.s.	98.9
3TMD homotypic interaction				
3TMD125-GFP + 3TMD125-Rluc	0.806 ± 0.071	5	<0.001	30.8
3TMD367-GFP + 3TMD367-Rluc	0.917 ± 0.061	6	<0.01	64.0
3TMDs heterotypic interaction				
3TMD125-GFP + 3TMD367-Rluc	0.806 ± 0.010	3	<0.001	46.3
3TMD367-GFP + 3TMD125-Rluc	0.885 ± 0.012	3	<0.05	64.7
3TMD–5TMD interaction				
5TMDΔ23-GFP + 3TMD125-Rluc	0.776 ± 0.020	4	<0.001	48.3
5TMDΔ23-GFP + 3TMD367-Rluc	0.877 ± 0.030	4	<0.01	73.3
5TMDΔ34-GFP + 3TMD125-Rluc	0.914 ± 0.041	4	<0.05	79.8
5TMDΔ34-GFP + 3TMD367-Rluc	1.009 ± 0.061	4	n.s.	103.0
5TMDΔ45-GFP + 3TMD125-Rluc	0.931 ± 0.024	4	<0.05	84.5
5TMDΔ45-GFP + 3TMD367-Rluc	0.937 ± 0.010	4	n.s.	86.5
5TMDΔ67-GFP + 3TMD125-Rluc	0.826 ± 0.031	4	<0.01	59.5
5TMDΔ67-GFP + 3TMD367-Rluc	0.892 ± 0.011	4	<0.05	75.8
3TMD125-GFP + 5TMDΔ23-Rluc	0.841 ± 0.088	4	<0.01	57.3
3TMD125-GFP + 5TMDΔ34-Rluc	0.819 ± 0.044	4	<0.01	52.8
3TMD125-GFP + 5TMDΔ45-Rluc	0.846 ± 0.049	4	<0.01	58.3
3TMD125-GFP + 5TMDΔ67-Rluc	0.824 ± 0.061	4	<0.01	53.0
3TMD367-GFP + 5TMDΔ23-Rluc	0.990 ± 0.041	5	n.s.	91.8
3TMD367-GFP + 5TMDΔ34-Rluc	0.989 ± 0.028	4	n.s.	93.8
3TMD367-GFP + 5TMDΔ45-Rluc	0.958 ± 0.042	4	n.s.	85.5
3TMD367-GFP + 5TMDΔ67-Rluc	0.984 ± 0.053	4	n.s.	91.8

[†]The average and standard deviation for the indicated number of independent experiments.
The statistical significance of each BRET efficiency was tested compared to the BRET signal of CXCR4-GFP and CXCR4-Rluc (Student's *t*-test). n.s., not significant.
[‡]The relative BRET efficiency was calculated for each experiment and the average is shown.

Table 4. Detection of higher-order multimerization of CXCR4 by bioluminescent resonance energy transfer (BRET)–bimolecular fluorescence complementation (BiFC) analysis

Sample	BiFC–BRET signal[†]	*n*	*P*-value
Specificity control			
mKGN 1000 ng + mKGC 1000 ng + Rluc	0.615 ± 0.070	3	
CXCR4 mKGN 500 ng + CXCR4 mKGC 500 ng + Rluc	0.624 ± 0.049	6	
CXCR3 mKGN 1000 ng + CXCR3 mKGC 1000 ng + CXCR3 Rluc	0.569 ± 0.021	3	
CXCR4–CXCR3 interaction			
CXCR3 mKGN 1000 ng + CXCR3 mKGC 1000 ng + CXCR4 Rluc	0.610 ± 0.065	3	n.s.
CXCR4 mKGN 31.3 ng + CXCR4 mKGC 31.3 ng + CXCR3 Rluc	0.593 ± 0.021	4	n.s.
CXCR4 mKGN 62.5 ng + CXCR4 mKGC 62.5 ng + CXCR3 Rluc	0.582 ± 0.011	4	n.s.
CXCR4 mKGN 125 ng + CXCR4 mKGC 125 ng + CXCR3 Rluc	0.586 ± 0.015	4	n.s.
CXCR4 mKGN 250 ng + CXCR4 mKGC 250 ng + CXCR3 Rluc	0.568 ± 0.011	4	n.s.
CXCR4 mKGN 500 ng + CXCR4 mKGC 500 ng + CXCR3 Rluc	0.573 ± 0.014	4	n.s.
CXCR4–CXCR4 interaction			
CXCR4 mKGN 31.3 ng + CXCR4 mKGC 31.3 ng + CXCR4 Rluc	0.634 ± 0.023	6	n.s.
CXCR4 mKGN 62.5 ng + CXCR4 mKGC 62.5 ng + CXCR4 Rluc	0.644 ± 0.035	7	n.s.
CXCR4 mKGN 125 ng + CXCR4 mKGC 125 ng + CXCR4 Rluc	0.676 ± 0.016	7	<0.05
CXCR4 mKGN 250 ng + CXCR4 mKGC 250 ng + CXCR4 Rluc	0.707 ± 0.030	7	<0.01
CXCR4 mKGN 500 ng + CXCR4 mKGC 500 ng + CXCR4 Rluc	0.717 ± 0.054	10	<0.01

[†]The average and standard deviation for the indicated number of independent experiments are shown.
The statistical significance of each BiFC–BRET signal was tested compared to the signal of CXCR4 mKGN + CXCR4 mKGC + Rluc (Student's *t*-test). n.s., not significant. The gray scale code represents the BRET efficiency: >100%, black; >80% dark gray; >60%, gray; >40%, light gray; >20%, white gray; <20%, white.

doi: 10.1111/j.1349-7006.2008.00997.x